SYNTHESIS AND CHARACTERIZATION OF SbSe THIN FILMS FOR PHOTOVOLTAIC APPLICATIONS

FOTOVOLTAİK UYGULAMALAR İÇİN SbSe İNCE FİLM SENTEZİ VE KARAKTERİZASYONU

KÜBRA ÇELEN

PROF. DR ABDULLAH CEYLAN

Supervisor

Submitted to

Graduate School of Science and Engineering of Hacettepe University

as a Partial Fulfillment to the Requirements

for the Award of the Degree of

Master of Science

in Nanotechnology and Nanomedicine.

2021

To good and bad times that I left behind…

ABSTRACT

SYNTHESIS AND CHARACTERIZATION OF SbSe THIN FILMS FOR PHOTOVOLTAIC APPLICATIONS

Kübra ÇELEN

Master of Science, Department of Nanotechnology and Nanomedicine

Supervisor: Prof. Dr. Abdullah Ceylan

December 2021, 63 pages

In this thesis study, synthesis and characterization of an alternative absorber, antimony selenide (Sb_2Se_3), layer for photovoltaic applications have been investigated. Synthesis of the Sb_2Se_3 thin films has been carried out in a two-step process where deposition of Sb metallic precursor film by RF magnetron sputtering on soda-lime glass (SLG) and molybdenum (Mo) coated SLG (SLG/Mo) substrates and a subsequent selenization of the deposited precursor films in a single zone tubular furnace are involved. Upon optimization of the sputtering conditions for the Sb growth, the effects of precursor thickness, selenization temperature, selenization time on the morphology and the structure of the synthesized Sb_2Se_3 thin films have been investigated by various techniques. Based on XRD and Raman analyzes, it has been understood that for a phase-pure complete selenization, the optimum selenization time is 150 min and the optimum selenization temperature is 250℃ for ~500 nm thick Sb precursor on SLG. However, for the same thickness Sb film on SLG/Mo, selenization temperature is kept constant but, optimum selenization time is needed to increase to 180 min. Raman spectra and XRD patterns of these samples have completely matched with orthorhombic Sb_2Se_3 structure.

Although surface morphologies of all the thick samples investigated by SEM have revealed in plane arrangement of rod-like Sb_2Se_3 grains, cross-sectional image of the phase pure thick sample by FIB-SEM unveiled the fact that the rod-like morphology is only at the very surface and does not extend into the depth of the sample. Moreover, it has been observed that the thickness of the sample has increased excessively from 500 nm of the precursor to 790 nm. Since a thick absorber layer reduces the transportation of charge carriers to counter electrodes, the precursor thickness is decided to be reduced to 250 nm and the selenization conditions have been optimized, accordingly. The optimum selenization time for 250 nm Sb on SLG is determined to be 150 min and the optimum selenization temperature is 250℃ by investigating the XRD patterns. According to XRD and Raman analysis, selenization time and temperature have been optimized as 150 min and 250 ℃ for 250 nm thick Sb thin film deposited on SLG/Mo. Surface morphologies of thin Sb_2Se_3 samples via SEM have shown vertical arrangement of rod-like grains as opposed to those of thick Sb_2Se_3 samples. As expected, the variation of the surface arrangement has reflected itself on the XRD patterns as the inverse changes of $I_{(211)}/I_{(002)}$ and $I_{(221)}/I_{(002)}$ peak ratios. It has been determined that there is no impurity phase in fully selenized samples on SLG substrate and the increasing atomic concentration of Mo also matches with the decreasing atomic concentration of the Sb and Se elements at depth profiles of fully selenized samples on SLG/Mo substrate by XPS. Sb:Se atomic ratio obtained by EDS for the completely selenized 250 nm Sb thin film on SLG/Mo is in close agreement with that of Sb_2Se_3. Optical behavior of the fully selenized thin and thick samples have been determined by photoluminescence (PL) spectroscopy and PL spectra of these samples have commonly acquired a sharp interband transition peak at 1.53 eV. Therefore, we have thoroughly determined the proper Sb precursor film thickness and the selenization conditions in a two-step synthesis process for obtaining the desired Sb_2Se_3 structure on SLG/Mo substrates to be utilized in solar cell architecture.

Key Words: Sb_2Se_3 thin film absorber layer, two-step production, RF magnetron sputtering, selenization

ÖZET

FOTOVOLTAİK UYGULAMALAR İÇİN SbSe İNCE FİLM SENTEZİ VE KARAKTERİZASYONU

Kübra ÇELEN

Yüksek Lisans, Nanoteknoloji ve Nanotıp A.B.D.

Danışman: Prof. Dr. Abdullah CEYLAN

Aralık 2021, 63 sayfa

Bu tez çalışmasında fotovoltaik uygulamalar için alternatif bir soğurucu tabaka olan antimon selenyumun (Sb_2Se_3) sentezi ve karakterizasyonu araştırılmıştır. Sb_2Se_3 ince filmlerinin sentezi, soda kireç camı (SLG) ve molibden kaplı SLG (SLG/Mo) alttaşlar üzerine RF magnetron sıçratma yöntemiyle ile Sb metalik öncül filmin biriktirilmesini ve ardından bu filmlerin tek bölgeli bir tüp fırın içerisinde selenizasyonunu içermektedir. Sb büyümesi için sıçratma koşullarının optimizasyonundan sonra, öncül film kalınlığı, selenizasyon sıcaklığı, selenizasyon süresinin sentezlenen Sb_2Se_3 ince filmlerin morfoloji ve yapısı üzerindeki etkileri çeşitli tekniklerle araştırılmıştır. XRD ve Raman analizine göre, SLG üzerine biriktirilmiş 500 nm film kalınlığı için optimum selenizasyon süresinin 150 dakika ve optimum selenizasyon sıcaklığının 250 °C olduğu anlaşılmıştır. Ancak, selenizasyon sıcaklığı değiştirilmezken, XRD ve Raman analizlerine göre SLG/Mo üzerine biriktirilmiş 500 nm film kalınlığı için optimum selenizasyon süresi 180 dakikaya

çıkarılması gerektiği anlaşılmıştır. Bu numunelerin Raman ve XRD verileri ortorombik Sb_2Se_3 yapısı ile tamamen eşleşmektedir.

Selenlenmiş kalın örneklerin (SLG ve SLG/Mo üzerine 500 nm Sb ince film) yüzey morfolojileri SEM ile incelendiğinde örneklerin yüzeyinde yatay rod benzeri yapıların olduğu görülmüştür. Tamamen selenlenmiş, yan fazlar içermeyen kalın örneğin FIB-SEM ile elde edilmiş kesit görüntüsü incelendiğinde, bu yatay rod benzeri yapının bütün bir kesitte değil, sadece örneğin yüzeyinde olduğu belirlenmiştir. Ayrıca örnek kalınlığının, öncül film kalınlığı olan 500 nm'den 790 nm'ye aşırı arttığı gözlemlenmiştir. Soğurucu tabaka kalınlığının fazla olması yük taşıyıcıların karşı eletroda ulaşma olasılığını azaltacağından dolayı öncül film kalınlığı 250 nm'ye düşürülerek selenizasyon deneyleri optimize edilmiştir. XRD analizi ile SLG üzerinde biriktirilmiş 250 nm kalınlığındaki film için optimum selenizasyon süresinin 150 dk ve optimum selenizasyon sıcaklığı 250 ℃ olduğu anlaşılmıştır. XRD ve Raman analizlerine göre SLG/Mo üzerine biriktirilmiş 250 nm Sb ince filmler için selenizasyon süresi 150 dk ve selenizasyon sıcaklığı 250 ℃ olarak optimize edilmiştir. SEM ile yüzey morfolojileri incelenen ince Sb_2Se_3 örneklerin kalın Sb_2Se_3 örneklere kıyasla dikey yönelimli rod benzeri tanelere sahip olduğu görüldü. Beklenildiği üzere, morfolojideki bu değişiklikler, örneklerin XRD desenlerinden elde edilen $I_{(211)}$ / $I_{(002)}$ ve $I_{(221)}$ / $I_{(002)}$ pik oranlarındaki değişikliklere yansımaktadır. SLG alttaş üzerine hazırlanmış örneklerin yapsında elementel olarak bir kusur bulunmadığı ve SLG/Mo alttaş üzerine hazırlanmış örneklerin kalınlık profilinde Mo elementinin atomik konsantrasyonu artarken, Sb ve Se elementlerinin atomik konsantrosyonunun azaldığı XPS ile belirlenmiştir. Tam selenizasyonu sağlanmış örneklerin atomik birleşme oranları EDS ile belirlenmiş olup, sitokiyometrik olarak Sb_2Se_3 yapısına en yakın örneğin SLG/Mo alttaş üzerine hazırlanmış ince örneğin olduğu görülmüştür. Tam selenizasyonu sağlamış ince ve kalın örneklerin optik bantları 1.53 eV olarak PL ile belirlenmiştir. Bu sonuçlara göre, günes hücresi mimarisinde kullanılacak olan, SLG/Mo alttaşlar üzerinde istenilen Sb_2Se_3 yapısını oluşturmak için iki aşamalı sentez kullanılarak, uygun Sb öncül film kalınlığı ve selenizasyon koşulları belirlenmiş oldu.

Anahtar Kelimeler: Sb_2Se_3 ince film soğurucu tabaka, iki aşamalı üretim, RF magnetron sıçratma, selenizasyon

ACKNOWLEDGMENTS

Firstly, I would like to express my deepest gratitude my supervisor Prof. Dr. Abdullah Ceylan for his guidance and valuable advice. It was a great chance and honor for me to carry out this thesis under his supervision. I will forever be grateful to him for his patience and support.

I would like to thank Prof. Dr. Şadan Özcan, Dr. Mehmet Burak Kaynar and Dr. Telem Şimşek, who have always supported me both scientifically and morally throughout my studies. They have always been a light to me in this work.

I would like to extend my sincere thanks to my friends at SNTG, Oğul Deha Kesik, Altuğ İlbay, Ali Rıza Yıldırım, Mustafa Rizalar and other friends whose names I cannot say. I feel very lucky to meet them and I will never forget our conversation about our studies.

A very special thanks to Ayça Mercan Çalışkan, my dear friend. I have always felt her support by my side in good and bad times. I will never forget the great times that we spent together.

I would like to thank Yağmur Çelebi, who was like my sister, who managed to put a smile on my face during my stressful times.

I would like to thank Gökçem Çelik for his love and being my biggest support. There are no words that could explain my feelings about him. He made my life beautiful and meaningful. He motivated me during difficult times when I needed it.

Finally, I would also like to give special thanks to my parents, Ömer and Hatice Çelen and my siblings Fahriye and Mustafa Selahittin Çelen for their support, encouragement, and unconditional love through my life.

CONTENTS

LIST OF FIGURES

LIST OF TABLES

LIST OF SYMBOLS AND ABBRAVIATIONS

d	Spacing Between the Parallel Crystal Planes
θ	Bragg Angle
nλ	X-ray Wavelength
a	Lattice Parameter
t_{Se}	Selenization time
m_{Se}	Selenium Powder Mass
T_{subs}	Substrate Temperature
T_{Se}	Selenium Source Temperature
P_{Ar}	Argon Pressure
PV	Photovoltaic
SLG	Soda-Lime Glass
SLG/Mo	Mo Coated Soda-Lime Glass
TK	Thick
TN	Thin
XRD	X-Ray Diffraction
RS	Raman Spectroscopy
SEM	Scanning Electron Microscopy
BSE	Backscattered Electrons
SE	Secondary Electrons
EDS	Energy Dispersive X-Ray Spectroscopy
XPS	X-Ray Photoelectron Spectroscopy
FIB-SEM	Focused Ion Beam-Scanning Electron Microscopy
FIB	Focused Ion Beam
PL	Photoluminescence

Eg	Band-Gap Energy
RF	Radio Frequency
DC	Direct Current
PCE	Power Conversion Efficiency

1. INTRODUCTION

Energy includes variety of forms such as potential, kinetic, thermal, elastic, electrical, chemical, and nuclear energy. Modern societies benefit from different types of energy in different fields by transforming these forms of energy into each other in various ways. Depending on the rapid development of technology, increasing of prosperity level and growth of human population, energy need of humanity is rising day after day. Depending on increasing demand for energy, the energy is one of the most difficult problems to solve for the 21st century. Today, more than 7 billion people live in the world and this number is predicted to reach 9 billion at 2040. The rapid increase in the living standards of countries with high populations such as China and India cause an increase in energy demand. Nowadays, most of the people need energy while meeting their basic needs such as heating, nutrition, communication and cleaning in their workplaces, homes, and schools.

Until the French Revolution, muscle power of the animals was one of the most important energy sources and at the same time, secondary energy sources were firewood. For this reason, areas which have high forest density were efficient regions in terms of energy sources. This situation is thought to be play critical role for political order of Europe at that time. Lack of the firewood which is used for melting the metals of cannons and weapons caused the energy crisis at societies at that period. However, despite of the existence of the coal which is one of the fossil fuels was thought as secondary energy source for a long time. At the specific regions of the Europe, lack of the firewood that causes energy crisis increased the value of coal as energy sources. After the industrial revolution, high energy density of the coal was an advantage for steel making production and development of this source gained speed [1].

Fossil energy sources come into existence from animal and plant remains that get changed due to the lack of oxygen since the prehistoric ages, so these sources do not regenerate in short time.

Fossil energy sources which based of organic carbon compound are a form of stored solar energy. Depending on the burning of these compounds with oxygen, energy exists as heat energy.

Today, commonly used fossil energy sources are natural gas, oil, and coal which are suitable for electricity generation due to their high energy density. By the year 2020, 63% of electricity production is provided by fossil fuels in the world [2]. In Turkey, the usage situation of fossil fuels (Fig. 1.1) is not different from the rest of the world. 98 % of natural gas which is spent for electricity production is imported from other countries such as Russia, Iran, and Azerbaijan. This situation indicates that Turkey has a foreign source dependency on energy production [3].

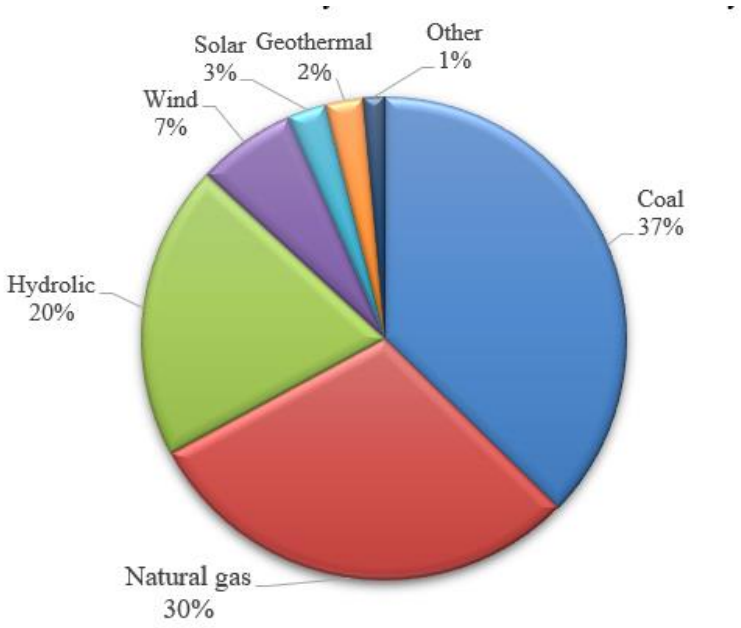

Figure 1.1. Distributions of electricity generation sources of Turkey in 2018

Several problems are come together by the usage of fossil fuels for energy production. One of these problems is the depletion of fossil fuel reserves depending on the rapid increase of energy consumption with the rising of the prosperity level. Fossil fuels are not regenerate in a short time period, so their percentage of presence in nature is decreased day by day. With this consumption rate, predictions indicate that coal in 119 years, natural gas in 60 and oil in 47 years will be depleted [4, 5]. Secondly, fossil energy sources cause

exhaust gas emissions during energy production. CO_2, NO_x, SO_x are waste products by virtue of the fossil fuels burning. Exhaust gases accumulate in the atmosphere and prevent balanced reflection of the incident light of the sun. This situation brings about a greenhouse effect that triggers global warming. The atmospheric concentration of CO_2 (see in Figure 1.2) is raised almost %48 due to human activities over the past 171 years [1, 6, 7].

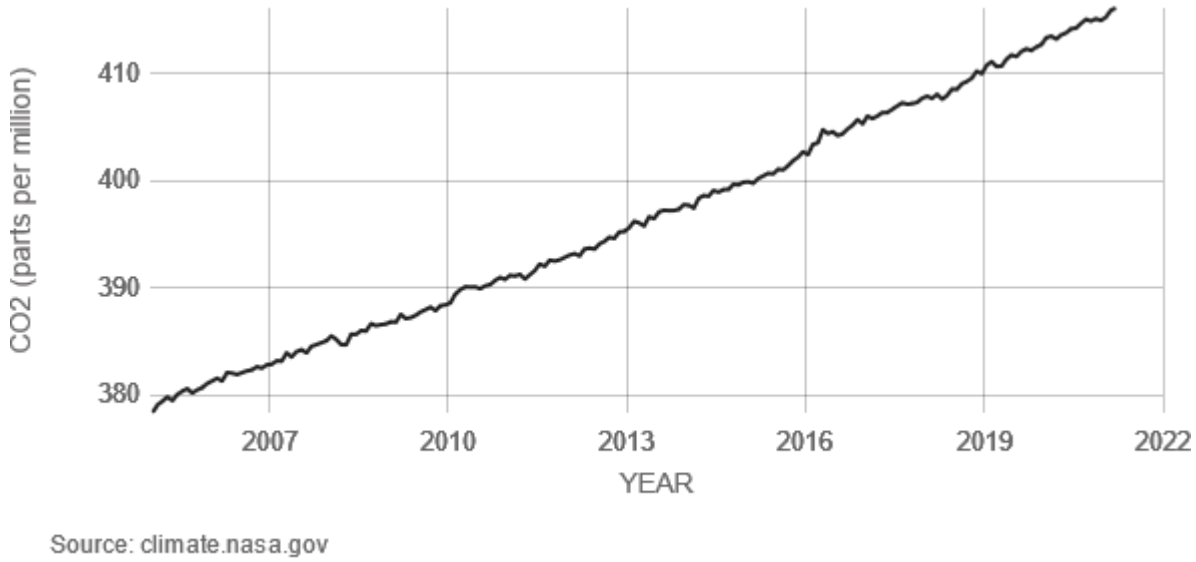

Figure 1.2. CO_2 emission level due to the year [7]

Since the use of fossil energy sources in energy production brings many problems, humanity needs alternative energy sources for a sustainable world.

Nuclear energy is obtained result of nuclear fusion or fission reactions. The heat that exists in consequences of fusion or fission reactions is used for electricity generation by the steam turbine. Nuclear energy is carbon-free energy, so it can be an alternative to fossil fuels. But nuclear energy has some disadvantages. It has very hazardous end products for human health and the environment. The storage of these waste products is still problematic. Elements that are used for nuclear reactions have a limited amount on earth [1, 8].

Hydropower is obtained from a turning water turbine depending on the water height and flow in a specific region. Electricity can be produced in this way wherever there is a stream. Hydropower plants supply 17 % of electricity around the world. Hydro energy is one of the carbon-free and renewable energy sources. However, this energy includes some challenges for the environment. Due to the barrage system, hydropower plants change the classic run of the river. As a result of the changes in living habitats, some species are becoming extinct. A huge amount of water reservoirs can cause floods which can destroy the living area of species [9].

Biomass energy is produced from organic waste. Organic components which are plants, agricultural and forestry residues, home waste, and animal waste can be used efficiently for energy generation. By using biofuels obtained from biomass or directly burning of biomass, heat and electricity production is provided. The net CO_2 emission of biomass energy is zero, so it is a carbon-free energy source. The widespread use of biomass for energy production has several disadvantages. The growth period of plants and the large area necessary for the growth of plants limit energy production [9, 10].

Wind power energy utilizes from the movement of air mass for energy production. Electricity generation from wind power is supplied from the flow of air which is the origin of mechanical energy that runs wind turbines and the generators. Wind energy is not harmful for the environment, and it has zero carbon emission. Wind energy is widely used in the European country. The construction cost of wind turbines is high. For energy production from wind turbines, they need the suitable intensity of the wind, so they cannot be built in every place [9, 10].

Geothermal energy involves energy production from hot water, steam, and gas that are occurred by accumulated heat in different depth levels of the earth's crust. Steam is separated from geothermal sources and by the usage of steam turbines, electricity is generated from geothermal energy. Electricity generation from geothermal energy does not include CO_2 emission, so it is an environmentally friendly energy source. The

temperature of geothermal sources is important for energy generation, so geographic region, topography, and drilling depth are critical [1, 9].

Sun is the fundamental energy source of earth. Solar energy systems are used to obtaining heat and electricity generation. Electricity generation from solar energy, there are two ways that are directly and indirectly. Direct electricity generation from solar energy, photovoltaic (PV) cells are used. Many types of materials have been developed for PV cells for generating electricity efficiently.

Commercially available PV cells are Si-based solar cells that are 80% percentage of the used around the world. However, they some disadvantages such as high production cost, low absorption coefficient, and high amount of material requirement. Thus, thin film solar cells can be replaced with Si-based solar cells. Thin film solar cell production requires low amount of material because of the thickness of the thin film, so their production cost is lower than the Si-based solar cells, and also, they can be deposited on flexible surfaces.

Thin fil solar cell consists of several layers that are absorber layer one of them. In thin film solar cell research, different types of absorber layer materials such as CdTe, CIGS, CZTS, CZTSSe, and SnS are used. These materials have some negative sides like including toxic and rare earth elements, unwanted secondary phase formation during the production, and low efficiency value. Sb_2Se_3 is one of the brilliant alternatives for absorber layer materials of thin film solar cells depending on the its optical absorption coefficient, proper bandgap, atmospheric stability, non-toxic and earth-abundant constituents.

In this study, the Sb_2Se_3 thin film structure will be synthesized by two-step production that includes sputtering Sb precursors and selenization of these precursors. Parameters of production steps will be optimized and synthesized thin films will be characterized by suitable methods. Due to the characterization results of the thin films, advantages and disadvantages of the production method for photovoltaic applications will be discussed.

2. THEORETICAL INFORMATION

2.1. Properties of the Sun Light

Every form of energy is converted from the sun's energy on the earth. Sun is responsible for hydropower, wind energy, fossil fuels, photovoltaic electricity, etc. depending on different energy conversion mechanisms, so energy which is obtained from the sun is the most abundant and permanent sustainable energy source of the world.

Electromagnetic energy is radiated in the form of photons which are light particles by the sun. Incident light of the sun is absorbed, reflected, and transmitted by the atmosphere before reaching the earth's surface. The incoming irradiation takes different shapes depending on the earth's geometry, its distance from the sun, astronomical coordinates, the composition of the atmosphere, and geographical location at any given point.

The light of the sun includes many different colors, so it looks white. Solar spectrum occurs from visible and invisible radiations and each of these radiations has different energy (Figure 2.1) [11]. It spreads over a wider spectrum of wavelengths from the short-wave infrared to ultraviolet.

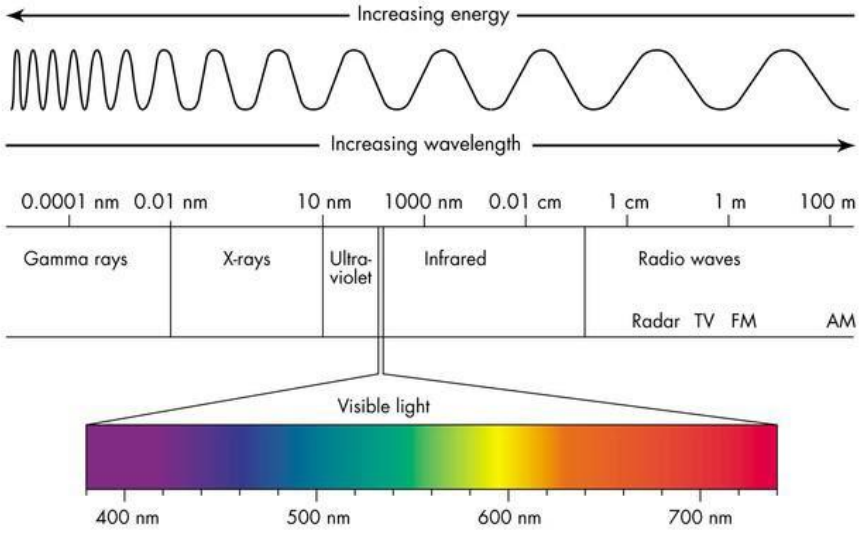

Figure 2.1. Electromagnetic spectrum [11]

Sun radiates a huge amount of solar energy from its surface into space with a power of $3.8x10^{23}$ kW and an only a small part of this energy reaches the earth's atmosphere. The solar radiation at the surface of the earth is about 1000–1200W/m^2 on a clear day and this small amount of energy supplies human needs several times [12, 13].

2.2. Solar Energy Harvesting

Solar energy that is almost distributed uniformly on the planet is free, silent and clean energy. Many systems have been developed to benefit from solar energy. These systems are used for generating heat and electrical energy by directly or indirectly using the heat and light coming from the sun. Solar heating systems that use the heat from the sun provide with space heating and hot water for buildings while thermal solar power plants and photovoltaic cells provide electricity with sun's heat and light.

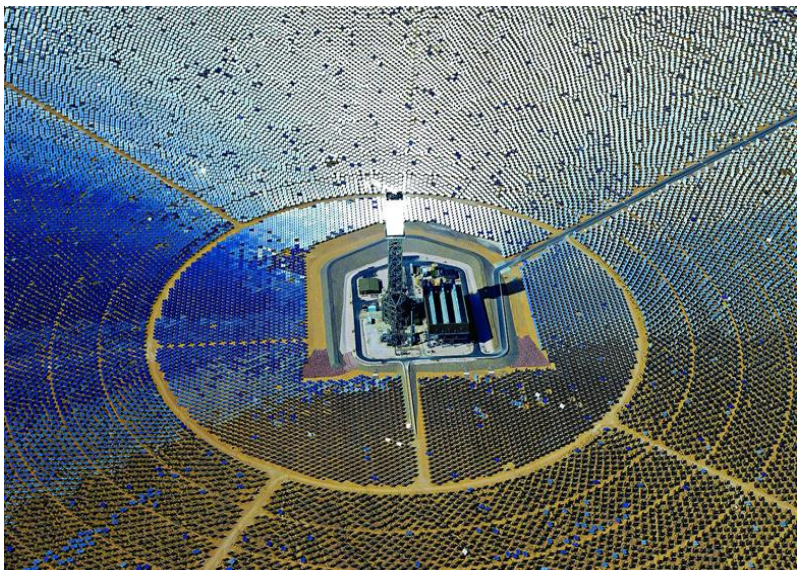

Figure 2.2. A typical Solar Tower Power Plant located at California [14]

Electricity production from solar energy is obtained two ways as directly and indirectly. Indirect electricity production is supplied solar-thermal systems. Solar-Thermal systems capture the solar radiation as heat and use this heat for electricity production via conventional thermal cycle. At these systems, solar reflectors concentrate the solar energy

on the central receiver. The vapor of the working fluid that is circulated through the system by a pump raises. Working fluid can be water, air, oil, liquid metal, molted salt, or diluted salt. Electricity is generated by turning steam turbine. One example of these systems is Solar Tower Power Plants which is showed Figure 2.2 [1, 9, 10, 14].

Direct electricity production from solar energy is supplied by photovoltaic cells. Photovoltaic solar cells enable to obtain of electrical energy with the photoelectric effect of semiconductors. The electrical energy conservation efficiency of solar cells depends on the characteristic of semiconductors. The efficiency values of commercial solar cells change 15 to 20% [10, 15].

2.3. Photovoltaic Effect

Photovoltaic cells convert the absorbed sunlight energy to electricity by the photovoltaic effect process. PV effect is based on electric potential difference generation at the junction of two different materials which are n-type and p-type semiconductor layers under the electromagnetic radiation.

A valence band electron is excited to the conduction band if the energy of the incident photon is equal to or higher than the bandgap of the semiconductor material. When an electron is excited to the conduction band by photon, it starts to move freely in the material, thus it leaves a hole behind, and electron-hole pairs have occurred. For preventing recombination of the electron with hole, an electric field is occurred by p-n junction that causes separation of positive and negative charges. Electric current and a voltage difference are created at semiconductor material due to p-n junction [16, 17].

2.4. Solar Cells

Electricity production from solar energy, one of the promising solutions to the world's energy need. The rapid development of the technology in the last 25 years has enabled to the production of PV cells more economically at large scale. There are many kinds of PV

cell technology that use different types of materials. Depending on the basic material usage of PV cell technologies are usually classified into three subtitles;

- First generation PV cells,
- Second generation PV cells,
- Third generation PV cells.

First generation PV cells include Si-based solar cells. Si is the most abundant second element on earth's crust. The first Si-based solar cell was developed by Bell Laboratories with 6% efficiency. More than 80% of commercial solar cells are Si-based that are produced electricity with 15% efficiency. Si has suitable bandgap energy that is 1.1 eV for PV applications. The production cost of the Si-based PV cell is high due to the row material purifying process. Si-based solar cells have a low optical absorption coefficient that is under 10^4 cm^{-1} [12, 18].

Second generation solar cells are known as thin film solar cells. The thickness of the thin film solar cells is almost a few micrometers. thin film solar cells distinguish with their features such as less material usage at cell production, lower cost, and shorter production time compared to Si-based solar cells. But, generally, efficiencies of thin film solar cells are lower than silicon solar cells, and earth rare and toxic elements can be used in their productions [19].

2.5. Thin Film Solar Cells

Thin film materials are produced by the random nucleation and growth processes of condensing, reacting atomic, and ionic molecular species on a substrate. Thin films may be produced wide thickness range, varying from a few nanometers to tens of micrometers. The properties of thin film material are strongly dependent on deposition parameters and also thickness of the material can affect the thin film properties. Thin films can be deposited on any type of substrate. Understanding thin film deposition processes clearly can help in achieving high-efficiency devices in large areas. Depending on these properties of the thin film material, thin film technologies are proper for solar cells.

Various materials and technologies are used to produce thin film solar cell fabrication. The advantages of thin film solar cells are lower manufacturing costs, reduced mass, short production time, reduced row material usage. Despite these advantages of the thin film solar cells, they have a lower efficiency value and increased toxicity in comparison with Si-based solar cells.

Thin film solar cell consists of several layers which are substrate, transparent conducting oxide layer, window layer, absorber layer, and metal contact layer. Each of these components has different physical and chemical properties and each affects the overall performance of the device [19, 20].

2.6. Absorber Layers

Absorber layer is most important part of thin film solar cell architecture. Electrons in the absorber layer are excited when the light falls on the solar cell. Excited electrons start to move freely in the solid. By the addition of the junction forming layer, electric field occurs in the structure. Due to the electric field, free electrons move to generate current. Thus, the absorber layer is central to the energy conversion process, so it must have a high absorption coefficient, low recombination rates, and high mobility for efficient charge collection. Several types of absorber layer materials such as CdTe, CIGS, CZTS, CZTSSe, and SnS are being investigated in thin film solar cell studies [21].

CdTe thin film solar cells have been started to develop after 1970s. The theoretically calculated efficiency of CdTe absorber layer is around 32% and its direct bandgap is 1.5 eV [22, 23]. The optical absorption coefficient of the CdTe absorber layer is higher than 10^3 cm^{-1} [24]. CdTe is a nontoxic compound, but it consists of Cd element that is toxic, so it can be harmful to the environment and human health. CdTe is generally 4-8 μm thick but Te is a rare earth element that causes high production costs [25].

CIGS is a suitable absorber layer material due to its high absorption coefficient that is higher than 10^5 cm^{-1} for thin film solar cells [26]. It has tunable direct bandgap 1.0 eV to

1.7 eV [27, 28]. During the last 5 years, CIGS has reached the high efficiency of 23.35% [29]. CIGS is a non-toxic environmentally friendly absorber layer material, but it has source materials limitations. Indium and gallium are rare earth elements and this situation increases the production cost of CIGS [25].

CZTS and CZTSSe are kesterite based absorber layer materials. They are promising absorber layer materials for thin film solar cells due to their non-toxic and earth-abundant constituents. They have a suitable bandgap and high absorption coefficient for solar energy harvesting. They have produced around 12% efficiency still far from the record efficiencies of CIGS and CdTe. CZTS and CZTSSe have phase control difficulty. Obtaining these materials as single-phase is problematic and they include secondary phases that are challenging for increasing efficiency [30-33].

SnS is an environmentally friendly absorber layer material because of its non-toxic constituents. SnS is composed earth-abundant elements, so production cost of an SnS based solar cell is relatively lower. The direct bandgap of SnS is 1.1 eV which is similar to Si. It has a high absorption coefficient above 10^4 cm^{-1}. SnS is a binary compound, so its phase control is simpler than CZTS and CZTSSe. The theoretically calculated efficiency value of SnS is 32%. Although these advantages properties of SnS, its record efficiency has so far reached to 4.4%. Because, when Sn reacts with S, several binary compounds as SnS_2, Sn_2S_3 that reduce the efficiency occur depending on the synthesis conditions [34-36].

2.7. Sb_2Se_3 as an Absorber Layers

Antimony selenide (Sb_2Se_3) is a promising alternative p-type absorber layer for thin film solar cells owing to its high absorption coefficient of 10^5 cm^{-1} in visible region of electromagnetic spectrum. It has 1.17 eV direct and 1.03 eV indirect bandgap at room temperature [37]. Sb_2Se_3 has high chemical stability, so it has a long serving life under atmospheric conditions. It has non-toxic and earth-abundant constituents which are relatively cheap. Theoretical calculations yield that the conversion efficiency of an Sb_2Se_3 based thin film solar cells can reach up to 30% [38, 39].

Sb_2Se_3 has an orthorhombic crystal structure which results in anisotropic material features and the properties change depending on the crystal directions. Unlike other inorganic absorber materials, Sb_2Se_3 acquires a 1D crystal structure, stacked parallel to the orthogonal direction, $(Sb_4Se_6)_n$ ribbons, minimizing the recombination rate at the grain boundaries due to the absence of dangling bonds. These ribbons are attached with weak van der Waals bonds along crystal directions of [010] and [100] and there are strong covalent bonds between Sb-Se atoms along [001] [40, 41].

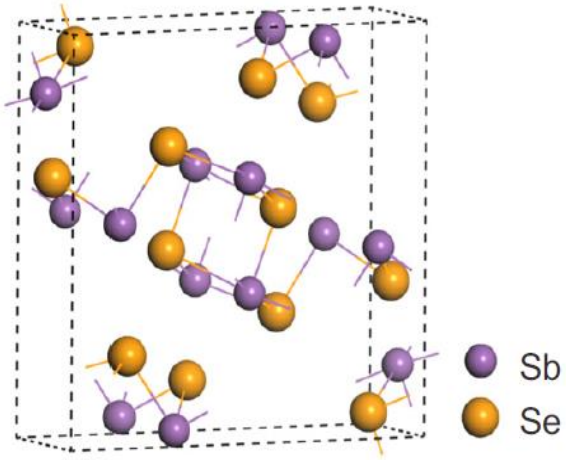

Figure 2.3. Crystal structure of Sb_2Se_3 [38]

Studies on Sb_2Se_3 thin film solar cells have gained speed for the last 5-6 years. The highest efficiency of 9.2% for Sb_2Se_3 based solar cells where the absorber layer deposited by close-spaced sublimation was reported by Li et al. in 2019 [41]. Sb_2Se_3 thin films can be produced directly by many physical and chemical methods such as;

- ✓ Sputtering [38, 42],
- ✓ Vapor transport deposition [43-45],
- ✓ Close-spaced sublimation [41, 46],
- ✓ Electrodeposition [47],
- ✓ Rapid thermal evaporation [40, 48].

Besides these methods, Sb_2Se_3 thin film absorber layer can be synthesized by two-step process which includes deposition of Sb precursor and selenization of the precursor. Sb_2Se_3 absorber layer is firstly synthesized by this way from Zhu et al. in 2016. DC magnetron sputtering was used for Sb thin film deposition from Sb target material. Following this step they applied selenization at different annealing temperatures for synthesizing the Sb_2Se_3 absorber layer with 0.72% PCE [49]. This team produced Sb_2Se_3 absorber layer by rapid thermal annealing with 3.47% PCE same year [50]. In 2019, %1.15 PCE was produced by Shen et al via e-beam evaporation of Sb and after that selenization of Sb thin film [51]. The highest efficiency as 6.84% PCE was obtained by the two-step method was reported by Luo et al. in July 2020. They synthesized Sb_2Se_3 absorber layer by using RF magnetron sputtering for deposition Sb thin film with different thickness and double-chamber vacuum tubular furnace for selenization [52]. Lastly, Liang et al published their study with 6.15% PCE in August 2020 and in this study a similar process to Zhu et al was followed [53].

3. EXPERIMENTAL SECTION

In this thesis study, we have utilized a two-step synthesis method where sputtering of metallic Sb precursors and selenization of the precursors are followed so as to eventually synthesize the Sb_2Se_3 structure. Initially, Sb precursor thin films are deposited by radio frequency (RF) magnetron sputtering technique and these precursors are selenized in a single-zone tubular furnace. Selenization at the different selenization times, effects of deposition on different structures, and effects of precursor thickness on structural growth of thin film have been examined. The structural analysis of synthesized thin films has performed by X-ray diffraction (XRD). Raman spectroscopy (RS) has been used for achieving more detailed information about phase analysis of Sb_2Se_3 thin films. Scanning electron microscopy (SEM) that is equipped with energy-dispersive x-ray spectroscopy (EDS) has been used for examination of surface morphology and elemental distribution of Sb_2Se_3 thin films. Examination of the cross-section of the sample has performed focused ion beam-scanning electron microscopy (FIB-SEM). The x-ray photoelectron spectroscopy (XPS) has been utilized for the detection of compositional depth profiles and investigating the purity of chemical states of the samples. Examination of the cross-section of the samples has performed focused ion beam-scanning electron microscopy (FIB-SEM). Determination of optical behavior of Sb_2Se_3 thin film has been accomplished by photoluminescence (PL) spectroscopy.

3.1. Synthesis of Sb_2Se_3 Thin Films

3.1.1. R.F. Magnetron Sputtering

One of the most commonly used techniques for thin film deposition is sputtering which has wide application areas such as semiconductor processing, surface finishing, and jewelry making. Basically, ionized atoms are accelerated to the surface of the target material and surface atoms of the target material are ejected at the sputtering process. Atoms that are ejected from the surface of the target material are condensed and nucleated on a substrate surface. The name of this process is sputtering deposition (Figure 3.1) [54, 55].

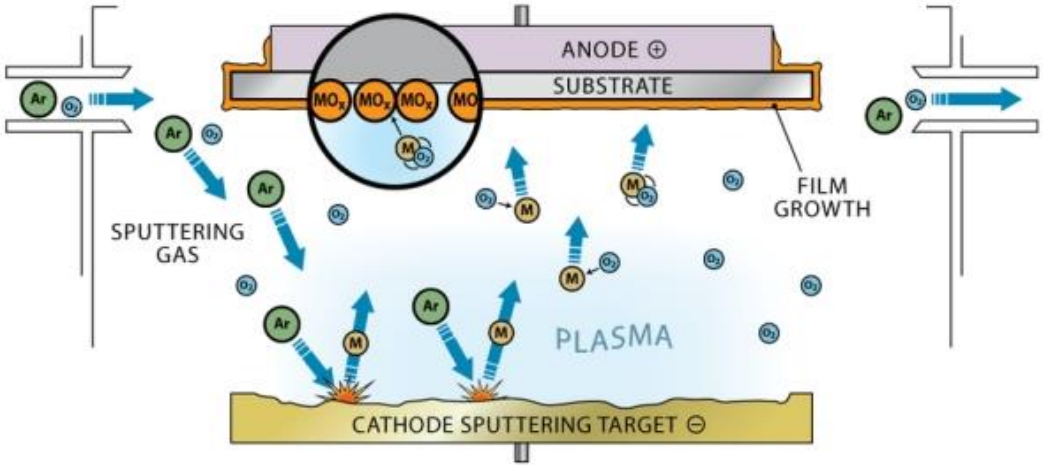

Figure 3.1. Sputtering process [55]

For obtaining ionized atoms, generally, Ar gas is used. A^+ ions are preferred due to their chemical inertness, low cost, and remotion easily from the sputtering system. Excitations of gas atoms are occurred by inelastic collisions that are between the energetic electrons and gas molecules Enough collision between the electrons and gas molecules supplies the plasma occurring. Partially ionized gas is called plasma. Some plasmas are glow discharges. Light emission from the excited atoms causes glowing [56, 57].

For producing a thin film by the sputtering method, targets are crucial that are commercially available. Targets can be made by all of the classes of solid such as metals, semiconductors, oxides, fluorides, borides, carbides, nitrides, silicides, and sulfates [58]. The sputtering process is separated into four main categories which names are DC, RF,

reactive, and magnetron. These categories can be combined with each other for enhancement sputtering efficiency.

Properly matching the target material classes with the sputtering process is important for sustainable glow discharge. Only conductive target materials can be sputtered by applying DC voltage. Insulating targets cannot be powered by DC voltage, because they act like capacitors. The surface of the insulating targets charges up with positive ions, so glow discharge cannot be sustained, and the sputtering process will stop. For a sustainable sputtering process with insulating targets, the DC power supply is replaced by an RF power supply. These kinds of sputtering systems are called RF sputtering systems [56, 59].

3.1.1.1. Preparation of Sb target material

Targets used through this study have been custom made out of Sb powder with 99.5% purity and 100 mesh purchased from Alfa Aesar Company. Carefully weighted Sb powder was filled in a 2-inch Cu baking cup and compressed by a hydraulic press (see Figure 3.2.a) for 72 hours under the 350 Barr pressure. As a result, the Sb target material which was shown in Figure 3.2.c was economically produced in comparison to commercially sold ones.

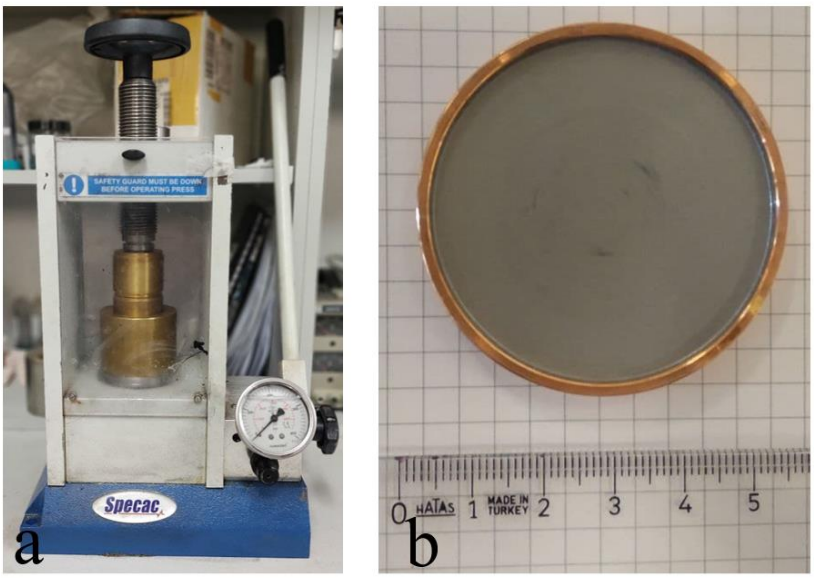

Figure 3.2 a) Hydraulic press, b) pressed Sb target

3.1.1.2. Deposition of Sb thin film

Sb thin films have been deposited on soda-lime glass (SLG) substrates and Mo thin film coated SLG substrates by RF magnetron sputtering technique. The sputtering system (see Figure 3.3.a) used for deposition of Sb thin film and its schematic view are given in Fig. 3.3. Before loading the SLG substrates to the vacuum system, SLG substrates have been cleaned by detergent, acetone, alcohol, and deionized water respectively. For homogeneous Sb precursor deposition, a rotating substrate holder has been used in the sputtering system. The distance between the substrate and the target is 13 cm. The base pressure of the sputtering vacuum chamber has pumped below 10^{-5} mbar, and the chamber was flushed with argon (Ar) three times so as reduce partial pressures of residual gases in the chamber. Deposition parameters of Sb thin films are presented in Table 3.1. Sb thin films have been deposited on SLG and SLG/Mo as ~250 and ~500 nm film thickness. t~500 nm and t~250 nm Sb metallic precursor thin films are respectively labelled as TK-Sb and TN-Sb.

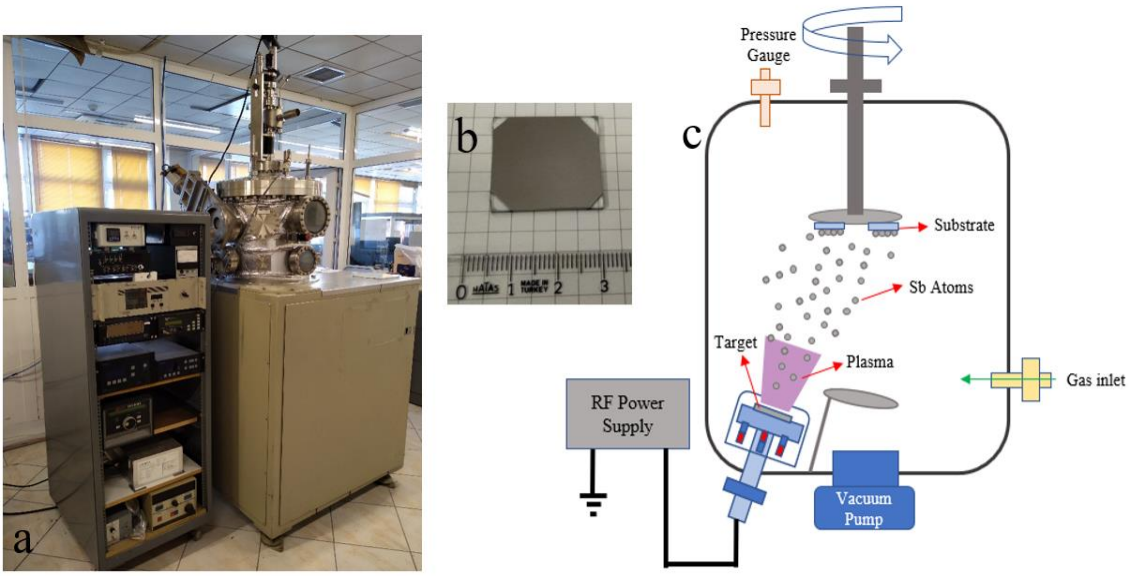

Figure 3.3. a) RF magnetron sputtering system, b) deposited Sb thin film, c) schematic illustration of the sputtering system.

Table 3.1. Deposition parameter of Sb precursors by RF magnetron sputtering method

	TK-Sb on SLG	TK-Sb on SLG/Mo	TN-Sb on SLG	TN-Sb on SLG/Mo
Time (min)	120	120	60	60
Thickness (nm)	~500	~500	~250	~250
RF Power (Watt)	40	40	40	40
Pressure $_{Ar}$ (mTorr)	8	8	8	8

3.1.2. Selenization

Selenization is a kind of thermal diffusion method which includes a surface of a material is exposed to a selenium containing atmosphere at relatively high temperature. Surface of the materials reacts with selenium and start to exist new compound from surface to inside of material.

In this study, selenization process of the Sb thin films has been performed under the 2 major groups.

- High Vacuum Selenization of Sb Thin Films
- Low Vacuum Selenization of Sb Thin Films

3.1.2.1. High vacuum selenization of Sb thin films

Firstly, selenization of the Sb precursors has been performed in a high vacuum system (see Figure 3.4). The system has a ceramic plate heater for sample heating and a ceramic crucible which is heated by a clamp heater for evaporation of Se powder. The high vacuum chamber has pumped below to10^{-5} Torr. After several optimization experiments, the evaporation temperature of Se powder has been determined as 250℃. For providing enough Se vapor during the experiment, the heating rate of the ceramic plate and Se crucible has been adjusted to the same time. High vacuum selenization parameters of Sb thin films have given at Table 3.2.

Table 3.2. High vacuum selenization parameters of TK-Sb

Sample Name	**HV-T250**	**HV-T275**	**HV-T300**	**HV-T325**
T_{subs} (°C)	250	275	300	325
T_{se} (°C)	250	250	250	250
t_{se} (min)	60	60	60	60
m_{se} (g)	0.3	0.3	0.3	0.3

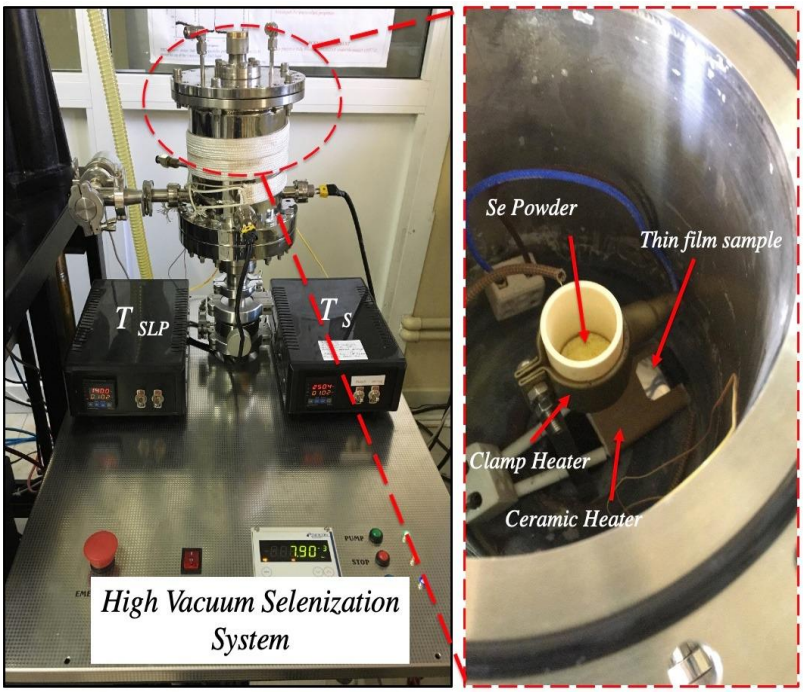

Figure 3.4. High vacuum selenization system

After all these experiments, according to XRD results (Fig. 3.5) of the samples, the selenization method of the Sb thin films has been changed. When XRD patterns of the samples is examined, all samples have just metallic Sb peaks. It has been understood from characterization results that all of the Se vapor has been removed by the high vacuum in the system.

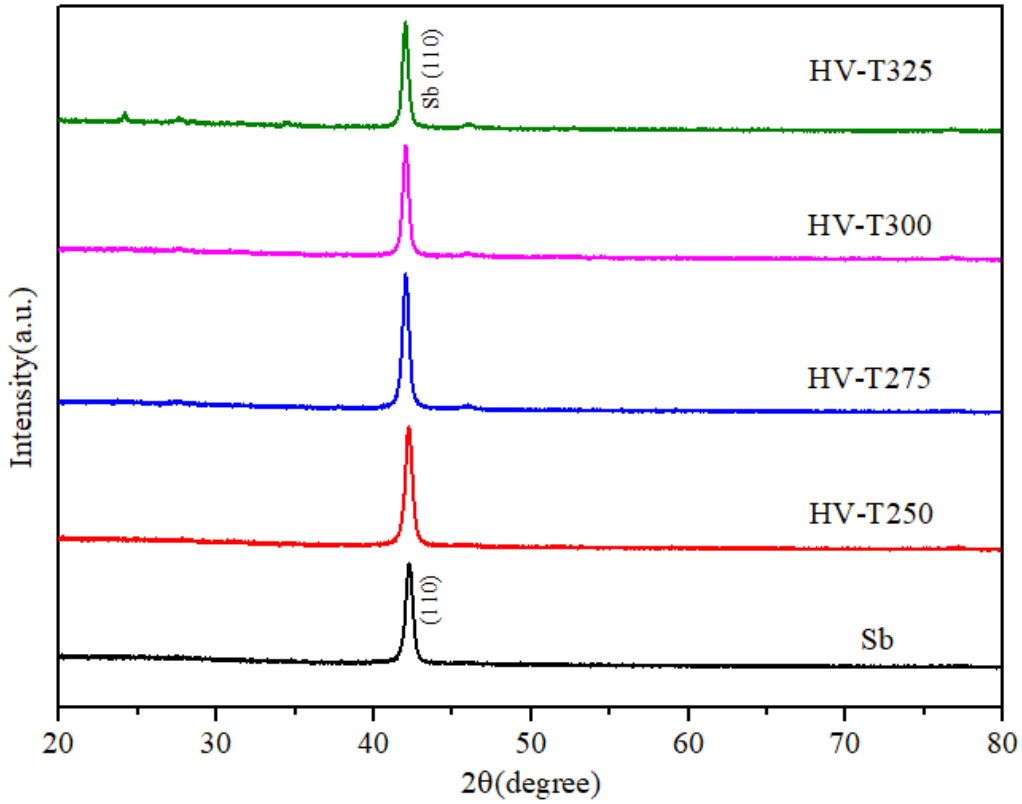

Figure 3.5. XRD patterns of the HV-T250, HV-T275, HV-T300, and HV-T325

3.1.2.2. Low vacuum selenization of Sb thin films

Selenization of the Sb thin films has been conducted via a conventional process which utilizes evaporation of Se powder in a cylindrical quartz tube under controlled flow of Ar carrier gas. The custom built selenization system used in this study is shown in Figure 3.6., Sb thin film samples and Se powder in a ceramic crucible are placed into the quartz tube with an appropriate positioning for adjusting the evaporation and selenization

temperatures of the Se powder and the sample, respectively. Quartz tube is pumped below 10^{-1} mbar using a rotary vacuum pump.

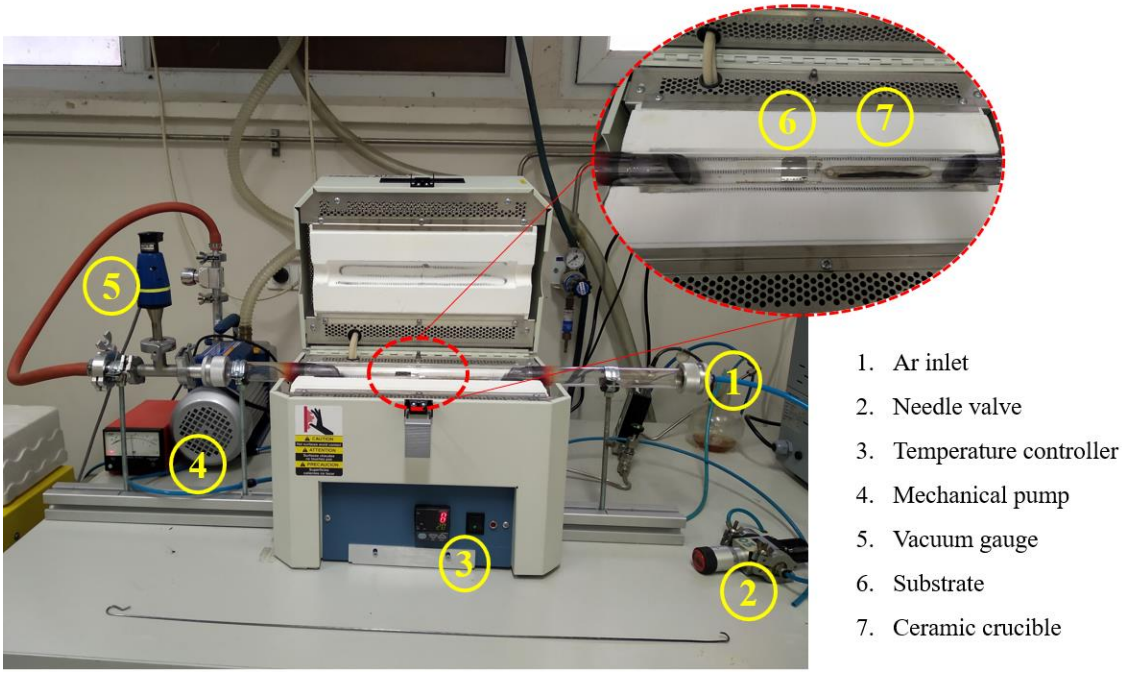

Figure 3.6. Low vacuum selenization system

Heating rate of the selenization system is adjusted at 7℃/min to achieve a setpoint. Substrate and Se crucible temperature are adjusted 250℃. Because of the same temperature of the substrate and Se crucible during the selenization, they have been

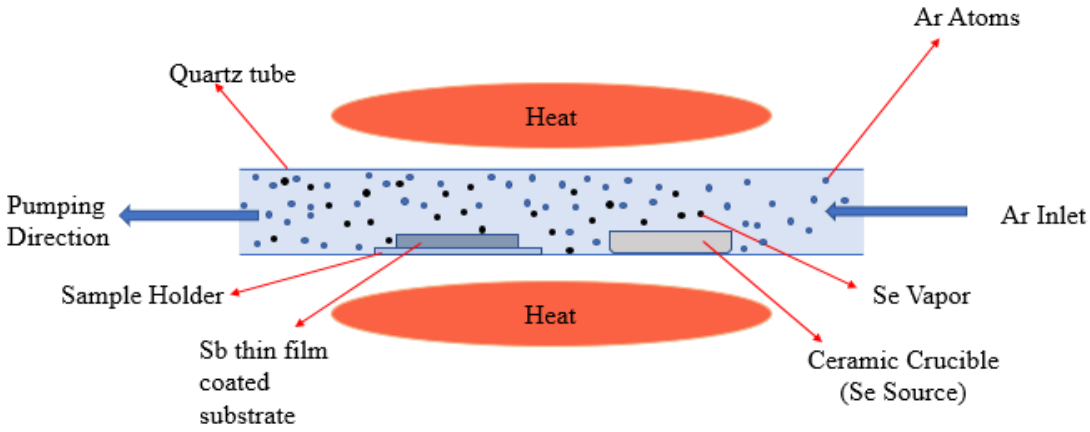

Figure 3.7. Schematic view of selenization process

located center of the tube furnace. Selenization time (t_{Se}) has been increased until sufficient t_{Se} is obtained for complete selenization. Complete selenization is critical because nonuniform phase distribution and local selenization of the structure affects the performance of thin film solar cell negatively. Depending on the t_{Se}, the amount of the selenium powder (m_{se}) in the crucible has been increased for preventing the absence of the selenium vapor in the system during the selenization. Se vapor has been carried in the quartz tube with help of the mechanical pump and Ar flow. Ar has been passed through the quartz tube from beginning to end of the selenization step which includes heating to selenization temperature and cooling to room temperature preventing from oxidation of samples. A vacuum gauge is used for determining Ar pressure in the quartz tube and Ar flow has been controlled by a needle valve. Furnace temperature has been naturally decreased to room temperature when the selenization step has finished. Schematic illustration of selenization process is given at Fig. 3.7.

Thick Sb precursors deposited by RF magnetron sputtering as ~500 nm on SLG (labeled as TK-Sb) have been used for selenization. t_{Se} has been chosen as 60, 90, 120, and 150 min for TK-Sb that have labeled SS60, SS90, SS120, and SS150. Selenization conditions of TK-Sb on SLG are given in Table 3.3.

Table 3.3. Selenization parameters of TK-Sb on SLG

Sample Name	**SS60**	**SS90**	**SS120**	**SS150**
t_{se} (min)	60	90	120	150
m_{se} (g)	0.50	0.75	1.00	1.50
T_{se} (^{o}C)	250	250	250	250
T_{subs} (^{o}C)	250	250	250	250
P_{Ar}(mTorr)	250	250	250	250

Mo thin film which is widely used as back contact material at thin film solar cells has been preferred for observation of growth behavior of SbSe structure above the different layer from the SLG. Sb precursors have been deposited on Mo coated SLG by RF magnetron sputtering as ~500 nm thickness which is named TK-Sb on SLG/Mo.

Depending on the presence of the Mo thin film layer on SLG substrate and because of the larger grain sizes of the Sb metallic precursor thin film, t_{se} has reached 180 min for complete selenization. Selenized TK-Sb on SLG/Mo has been named Mo-SS60, Mo-SS90, Mo-SS120, Mo-SS150, and Mo-SS180. Selenization conditions of TK-Sb on SLG/Mo are given in Table 3.4.

Table 3.4. Selenization parameters of TK-Sb on SLG/Mo

Sample Name	**Mo-SS60**	**Mo-SS90**	**Mo-SS120**	**Mo-SS150**	**Mo-SS180**
t_{se} (min)	60	90	120	150	180
m_{se} (g)	0.50	0.75	1.00	1.50	1.50
T_{se} (°C)	250	250	250	250	250
T_{subs} (°C)	250	250	250	250	250
P_{Ar}(mTorr)	250	250	250	250	250

Thin Sb precursors which are deposited by RF magnetron sputtering as ~250 nm thickness (labeled as TN-Sb) have been used for selenization experiments for examination of structural and morphological effects of precursor thickness. t_{se} has been selected 60 min initially, and t_{se} has increased to 150 min for complete selenization at different samples. Selenized TN-Sb on SLG has labeled S60, S90, S120, and S150 Selenization conditions of TN-Sb on SLG precursors are given in Table 3.5.

Table 3.5. Selenization parameters of TN-Sb on SLG

Sample Name	S60	S90	S120	S150
t_{se} (min)	60	90	120	150
m_{se} (g)	0.50	0.75	1.00	1.50
T_{se} (°C)	250	250	250	250
T_{subs} (°C)	250	250	250	250
P_{Ar}(mTorr)	250	250	250	250

Sb precursors have been deposited on Mo coated SLG by RF magnetron sputtering as ~250 nm thickness which is named TN-Sb on SLG/Mo. t_{se} has reached 150 min for complete selenization. Selenized TN-Sb on SLG/Mo has been named Mo-S60, Mo-S90, Mo-S120, and Mo-S150. Selenization conditions of TN-Sb on SLG/Mo are given in Table 3.6.

Table 3.6. Selenization parameters of TN-Sb on SLG/Mo

Sample Name	Mo-S60	Mo-S90	Mo-S120	Mo-S150
t_{Se} (min)	60	90	120	150
T_{subs} (°C)	250	250	250	250
T_{se} (°C)	250	250	250	250
m_{se} (g)	0.50	0.75	1.00	1.50
P_{Ar}(mTorr)	250	250	250	250

3.3. Characterization Methods of Synthesized Thin Films

In this thesis SbSe thin films were analyzed by using various characterization techniques;

- ✓ X-Ray Diffraction (XRD)
- ✓ Raman Spectroscopy (RS)
- ✓ Scanning Electron Microscopy (SEM)
- ✓ Focused Ion Beam -Scanning Electron Microscopy (FIB-SEM)
- ✓ X-Ray Photoelectron Spectroscopy (XPS)
- ✓ Energy Dispersive X-Ray (EDS)
- ✓ Photoluminescence (PL) Spectroscopy

In this section, brief information about these techniques is given.

3.3.1. X-Ray Diffraction

XRD is the most powerful method for determining the crystallographic and molecular structural properties of materials without destruction in solid forms. Structural properties such as grain size, strain, phase composition, preferential orientation can be determined by this method.

X-rays are a part of the electromagnetic spectrum that have wavelengths from 1 to 100 Å, however, only 0.3 to 2.5 Å is used for x-ray diffraction. X-ray diffraction methods generally work with single wavelength x-ray radiation sources which are called monochromatic x-ray radiation. For obtaining monochromatic radiation, x-rays must be also filtered out of the other radiations from the x-ray band [60-62].

Bragg's Law which is given at Equation (1) describes the x-ray diffraction. This law is related to interspacing between atomic planes that have periodic structures. Bragg's Law is obtained easily from the calculation of the path differences between two beams. The spacing between the parallel crystal planes (d) and incident angle (θ) with the same (hkl) affect the path difference. The path difference must be equal to one or multiple X-ray wavelengths ($n\lambda$) for keeping these beams in the same phase.

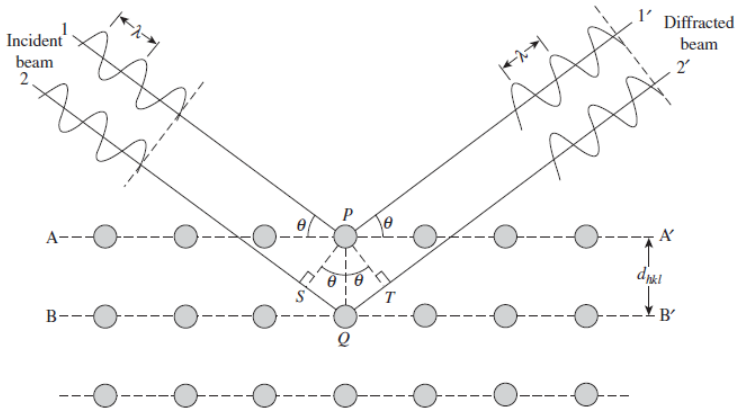

Figure 3.8. Diffraction of x-rays by planes of atoms

$2d\sin\theta = n\lambda$ *Bragg's Law*..... *Equation (1)*

Due to Bragg's Law, information is obtained about the spacing between atomic planes of a crystal by detection constructive interference at the incident angle and a wavelength of the incident beam. Determining the crystal structure of materials is provided by knowing the spacings of crystallographic planes by diffraction methods (in Fig. 3.8). Relation between the plane spacing of cubic crystal system and the related lattice parameter (*a*) is given at Equation (2).

$$d_{hkl} = \frac{a}{\sqrt{h^2+k^2+l^2}}$$ ..... *Equation (2)*

For calculating interplanar spacing of orthorhombic crystal structure, Equation (3) is used.

$$\frac{1}{d_{hkl}^2} = \frac{h^2}{a^2} + \frac{k^2}{b^2} + \frac{l^2}{c^2}$$ ..... *Equation (3)*

In this work, the structural analysis of synthesized and deposited thin films has been performed by Rigaku D-Max B XRD system with CuK_α radiation under operation conditions 20^o to 80^o at SNTG Laboratory in Hacettepe University.

3.3.2. Raman Spectroscopy

RS is a valuable technique for the molecular characterization of materials in the fact that obtaining a physical and chemical fingerprint of materials. RS has extreme sensitivity to the molecular environment of materials. Information that is obtained from molecular vibrations of the material can provide about the structural, orientational, and chemical properties of the material. RS is utilized to get detailed structural information of amorphous materials when compared to the XRD. This technique is also used for detecting impurities and secondary phases in materials.

RS is based on light scattering phenomena. When a monochromatic laser source irradiates the sample surface, scattered light is observed that can be classified as Rayleigh, Stokes, and Anti-Stokes scattering. Most of the scattered light is Rayleigh scattering which occurs depending on the elastic collision of a photon with a molecule. At Rayleigh scattering, incident light energy equals scattered light that occurs in a molecular system. The probability of inelastic collision of the incident photon with a molecule is less. Scattered photons can have higher or lower energy due to the incident photon. Stokes scattering is detected when the incident photon has higher energy than the scattered photon due to transferring the part of its energy to the molecule. Anti-Stokes scattering is observed while the incident photon has lower energy than the scattered photon [62-64].

RS of our thin film samples has been performed utilizing a 532 nm green laser of a Jasco NRS-4500 Raman system at MERLAB of Yıldırım Beyazıt University.

3.3.3. Scanning Electron Microscopy

Scanning electron microscope is the most extensively utilized type of electron microscope that uses electrons as image generating source. Analysis with SEM is performed by using the interactions that occur as a result of sending electrons which are focusing on the surface of the material from an electron gun. Electron beam can be focused in nm size, so detailed and high-resolution images can be obtained for examinations of materials. SEM provides to get topological and compositional information from the material.

Basically, image generation in SEM is based on signals detection and analyzing these signals which result from the elastic and inelastic interactions of the electron beam with the material surface. Elastic scattering generates *Backscattered Electrons* (BSE) that are scattered from the atoms. These electrons conserve 60-80 % percent of their energies after the scattering. Inelastic scattering of the electrons from the sample produces *Secondary Electrons* (SE). SE have less energy compared to the BSE. Morphological and topological information is obtained from the SE and BSE are used for demonstrating the contrasts in multiphase samples composition [60, 62].

In this work, examination of surface morphology has been carried out by SEMs which are located at Yıldırım Beyazıt University MERLAB and Bilkent University UNAM.

3.3.4. Focused Ion Beam-Scanning Electron Microscopy

Focused ion beam (FIB) technology is generally utilized for four basic aims as milling, deposition, implantation, and imaging. FIB system generates high-energy ionized atoms of relatively big elements and focuses these atoms onto the sample surface. The sample surface is etched or milled easily due to the greater mass of the ions. The ion beam is used for different aims as well, including the deposition of the material above the sample. The ion beams strike atoms onto the surface of the sample and intermolecular attractions fix them into a surface. And also, FIB is preferred for the preparation of transmission electron microscopy samples due to its great etching capabilities [65].

FIB-SEM may be used for imaging cross-sectioning of the sample. The sample is etched with an ion beam vertically in a controlled manner. The sample is tilted with a determined angle and cross-section visualization is performed by SEM. If the sample includes different layers, these layers can be observed and their thickness can be determined [66].

In this study, the FIB-SEM technique is performed for examining a cross-section of the sample which is completed full selenization with FEI Nova NanoLab 600i SEM/FIB which has employed with 30kv and 0.93nA Ga^+ ion at UNAM in Bilkent University.

3.3.5. X-ray Photoelectron Spectroscopy

XPS is used for elemental analysis of surfaces, analyzing elemental distribution in a depth profile for thin films, and chemical state identification of solid samples. XPS detects photoelectrons that are ejected from one of the core electronic levels by incident X-ray photons [62].

In XPS, x-ray photon irradiates on the sample surface in a high vacuum atmosphere. Interaction between incident x-ray photon and sample surface causes ejection of the photoelectrons from core electronic level of surface atoms. Emitted photoelectrons energy is detected by the electron spectrometer. The binding energy of an electron identifies the atom and orbital that emit the electron [67, 68]. The depth-composition profile from XPS is obtained by etching the material surface with inert gas ions for a certain period of time and obtaining elemental information from the new surface that emerges [62].

Detection of compositional depth profiles and investigating the purity of chemical states of the samples has been carried out by Thermo Avantages XPS which has employed with Al K_α monochromatic X-ray source (1486.7 eV) at UNAM in Bilkent University.

3.3.6. Energy Dispersive X-Ray Spectroscopy

EDS that is generally equipped in SEM is used to get chemical information or elemental analysis of the materials. The working principle of EDS based on the interaction of the sample with focused electron beam. EDS detects the energy and intensity of the characteristic x-ray that is obtained from electron beam-sample interactions. Collecting x-ray signal supplies information about elemental composition and concentration from the selected area of the sample [69].

3.3.7. Photoluminescence Spectroscopy

PL spectroscopy is one of the significant optical characterization techniques. PL is a strong technique for examining the electronic structure of semiconductor materials that can be extrinsic or intrinsic. PL spectrum gives some information about crystal quality and purity.

In the fundamental mechanism of PL, a semiconductor is illuminated by a light source. If photon energy of light is greater than the band-gap energy (Eg) of the material, electrons are crossed from the valance band to the conduction band, and they leave holes in the valence band. When recombination occurs between electron-hole pairs, a photon that has a wavelength characteristic of the material and the particular radiative process is emitted. PL extracts information about the electronic structure of the material by the spectrum of light emitted from the material [63, 70, 71].

PL spectroscopy of the samples in this study has been obtained by Nanometrics RPM Blue at NANOTAM, Bilkent University.

4. RESULTS

In this section, we present characterization results for the deposited Sb thin films and SbSe thin films synthesized after selenization under various conditions. We have analyzed the effects of precursor thin film thickness (t~500 nm, labelled as TK-Sb: t~250 nm, labelled as TN-Sb) on the morphology of selenized samples. Moreover, TK and TN precursors have been deposited on (500 nm) Mo thin film coated SLG substrates. Therefore, in the first part, structural information of Sb precursor films is given. Second part of this section explains effect of selenization conditions on the formation of Sb_2Se_3 thin films for TK-Sb deposited on SLG and SLG/Mo substates and TN-Sb deposited on SLG and SLG/Mo.

4.1. Characterization Results Precursor Sb Thin Films

Sb metallic thin films deposited by RF magnetron sputtering as 250 and 500 nm thick have been examined by XRD. XRD patterns (not shown here) of both TN-Sb and TK-Sb have shown that these thin films have an amorphous crystal structure. Surface morphologies of the Sb precursor samples have been investigated by SEM in order to understand the granular structure of the samples in terms of size and shape distribution of the Sb grains.

Fig. 4.1 shows the surface morphology and particle size distribution histograms of Sb metallic thin films which are deposited by RF magnetron sputtering as ~500 nm and ~250 nm thick on SLG and SLG/Mo substrates that are examined with SEM. The surfaces of Sb metallic thin films constitute uniform small grain which can help low temperature selenization. Figure 4.1a indicates the surface morphology of TK-Sb on SLG, and the average particle diameter of this precursor thin film is 64.97 nm. When SEM image of the TK-Sb on SLG/Mo is examined in Fig 4.1c, TK-Sb on SLG/Mo has larger grains than TK-Sb on SLG and the average particle diameter of this precursor thin film is 94.92 nm. Depending on the shorter sputtering time, TN-Sb on SLG has smaller grains than TK-Sb on SLG that are indicated in Fig 4.1e. and it has 45.35 nm mean particle diameter. Fig. 4.1g indicates surface morphology of TN-Sb on SLG/Mo. It is clear that TN-Sb on SLG/Mo has larger grains than TN-Sb on SLG and the mean particle diameter of TN-Sb

on SLG/Mo is 67.54 nm. According to these data, precursor films that are deposited on SLG/Mo substrate have larger grains than precursor films which are deposited on SLG of the same thickness. The presence of the Mo layer on the surface of the SLG substrate has reduced the required energy for grain growth during the deposition of the precursor films. Therefore, Sb metallic precursor thin films that are deposited on SLG/Mo substrate have larger grains. These growth behaviors of Sb metallic precursor thin films can affect its selenization.

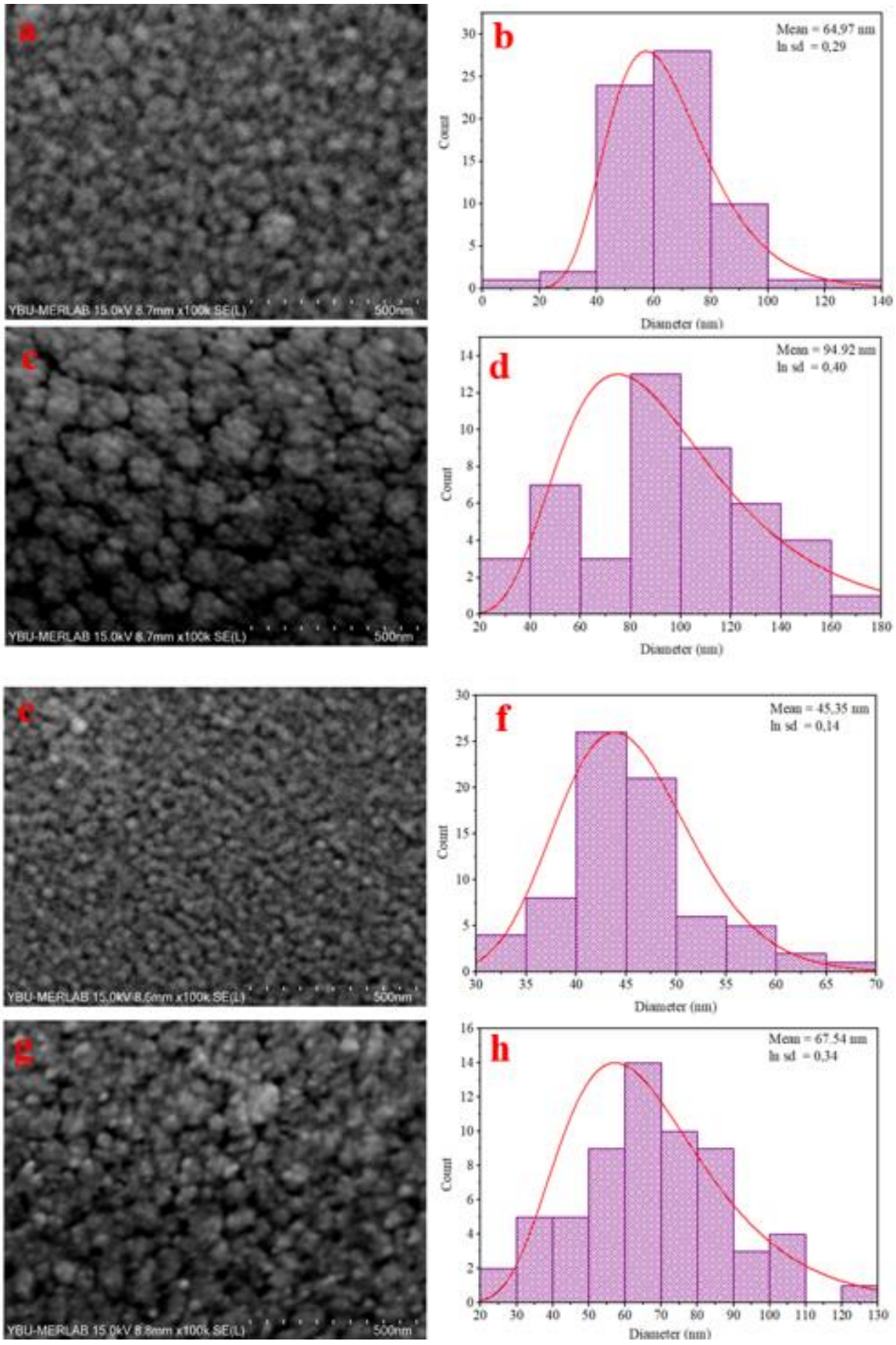

Figure 4.1. a) SEM image and b) grain size distribution of TK-Sb on SLG, c) SEM image and d) grain size distribution of TK-Sb on SLG/Mo, e) SEM image and f) grain size distribution of TN-Sb on SLG, g) SEM image and h) grain size distribution of TN-Sb on

4.2. Characterization Results of Selenized Sb Films

Selenized Sb films that are deposited by RF magnetron sputtering on SLG as ~250 nm and ~500 and SLG/Mo as ~250 nm and ~500 nm thick have been characterized by various methods. Characterization results of the selenized thick Sb films, which are shortly named TK-Sb_2Se_3, on SLG and SLG/Mo are given in the first part of this section. Structural analysis of TK-Sb_2Se_3 on SLG and SLG/Mo samples have been performed by XRD and RS and surface morphology investigation of these samples has been utilized by SEM. XPS, EDS, and PL have been used for analyzing complete selenized samples which are synthesized on SLG and SLG/Mo that are SS150 and Mo-SS180. XPS has been utilized for investigating the purity of chemical states of the SS150 and detection of the compositional depth profile of the Mo-SS180. Elemental compositions of SS150 and Mo-SS180 have been determined by EDS. The optical behavior of the SS150 and Mo-SS180 samples has been investigated by PL spectroscopy. Examination of the cross-section of the SS150 has performed FIB-SEM. In the second part of this section, characterization results of the selenized thin Sb films, which are shortly named TN-Sb_2Se_3, on SLG and SLG/Mo are given. XRD and Raman spectroscopy have been used for structural characterization and SEM has been utilized in the morphological investigation of TN-Sb_2Se_3 on SLG and SLG/Mo samples. As in TK-Sb_2Se_3, PL, EDS, and XPS have been used to characterize fully selenized samples which are synthesized on SLG and SLG/Mo that are S150 and Mo-S150. Chemical states purity investment of S150 and compositional depth profile detection of Mo-S150 has been performed by XPS. EDS has been used for determining the elemental compositions of S150 and Mo-S150. PL spectroscopy has been utilized for investigating the optical behavior of S150 and Mo-S150.

4.2.1. TK-Sb_2Se_3 on SLG and SLG/Mo

XRD patterns of the samples that are deposited on SLG substrate as ~500 nm Sb thin film precursor and selenized at different t_{Se} have been given in Figure 4.2. Diffraction peaks that are completely matched with orthorhombic Sb_2Se_3 crystal structure have been detected depending on the PDDF#00-015-0861 data. At SS60, besides the orthorhombic Sb_2Se_3 crystal structure peaks, a peak is observed at 2θ equal to 41.9° which belongs to (110) oriented rhombohedral Sb phase. Dominant peaks of the SS60 are (101), (230),

(240), and (002) oriented, and (240) oriented peak has the highest intensity of this sample. By increasing t_{Se}, except the (002) peak, intensities of other peaks have been decreased at SS90, SS120, and SS150. When the XRD pattern of the SS150 is examined, the dominant peak of the structure is (002) oriented, and (110) oriented Sb peak has been eliminated.

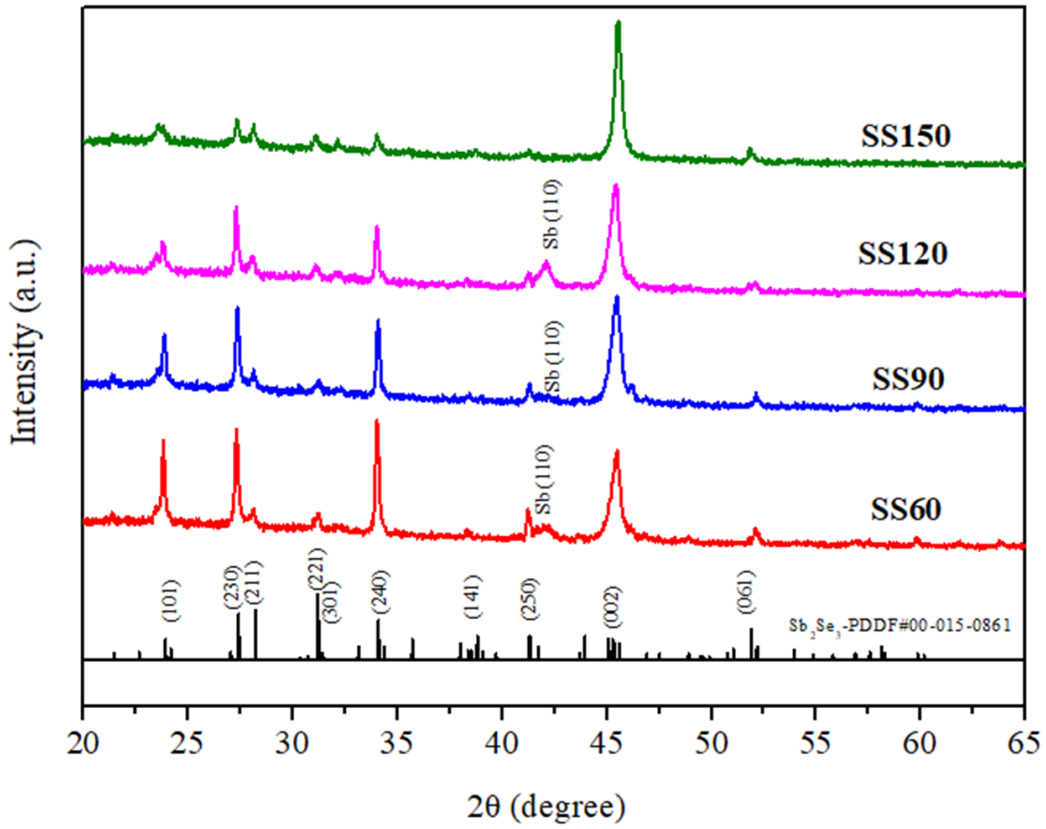

Figure 4.2. XRD patterns of the SS60, SS90, SS120, SS150

Fig. 4.3 represents the XRD patterns of the TK-Sb_2Se_3 on SLG/Mo at different t_{Se}. Diffraction peaks of the TK-Sb_2Se_3 on SLG/Mo are matched with orthorhombic Sb_2Se_3 structure and include Mo (110). At Mo-SS60, the diffraction pattern includes Sb (110) peak beside the orthorhombic Sb_2Se_3 and includes Mo (110). Diffraction peaks that belong to the orthorhombic Sb_2Se_3 structure have low intensity at Mo-SS60 when they have compared to the diffraction peak intensity of the other samples. By increasing $t_{Se,}$ the intensity of all structural peaks of orthorhombic Sb_2Se_3 has been raised. However, at Mo-SS180, dominant peaks of the structure have been changed. Dominant peaks of Mo-SS60, Mo-SS90, Mo-SS120, and Mo-SS150 have (230), (240), and (002) orientations

which belong to the Sb_2Se_3 structure. When the XRD pattern of Mo-SS180 is examined, it is observed that dominant peaks have changed, and (230) and (240) oriented peaks have been eliminated.

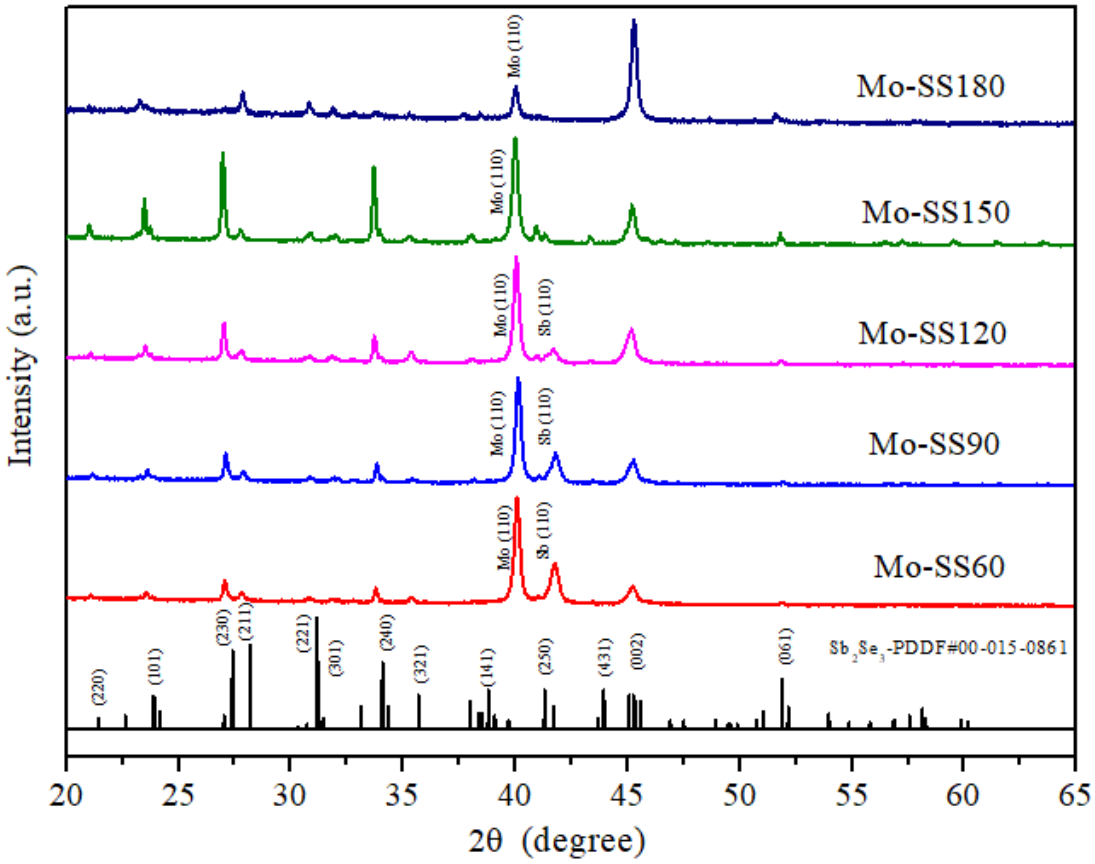

Figure 4.3. XRD patterns of the Mo-SS60, Mo-SS90, Mo-SS120, Mo-SS150, and Mo-SS180

In Fig 4.4, Raman spectra of samples which are deposited on SLG substrate as 500 nm Sb thin film precursor and selenized at different t_{Se}. Raman spectra that are performed by 532 nm laser excitation of samples were demonstrated for the further investigation of crystalline phases. All samples have a significant peak of around 187 cm^{-1} and two weak peaks around 121 cm^{-1} and 207 cm^{-1}. All peaks directly match with orthorhombic Sb_2Se_3 and the peaks at 187 cm^{-1} and 207 cm^{-1} assigned to the heteropolar Sb-Se bond vibrations.

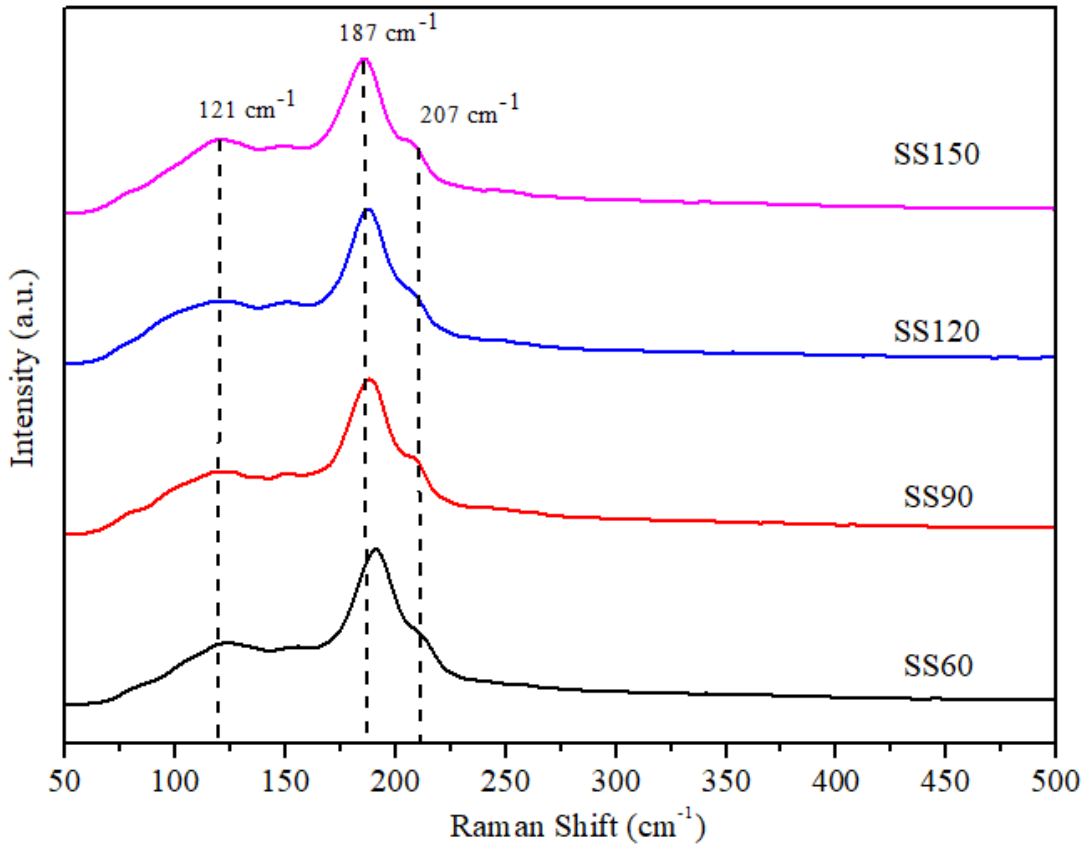

Figure 4.4. Raman spectra of the SS60, SS90, SS120, and SS150

RS results of TK-Sb_2Se_3 on SLG/Mo at different t_{Se} are given in Fig. 4.5. Raman spectra of TK-Sb_2Se_3 on SLG/Mo samples have been similar to Raman spectra of TK-Sb_2Se_3 on SLG samples. Raman shift has been obtained around the 121 cm^{-1}, 187 cm^{-1}, and 209 cm^{-1} which are related to orthorhombic Sb_2Se_3. The peaks at 187 cm^{-1} and 209 cm^{-1} have been assigned to the heteropolar Sb-Se bond vibrations. Unwanted secondary phase formation is not observed.

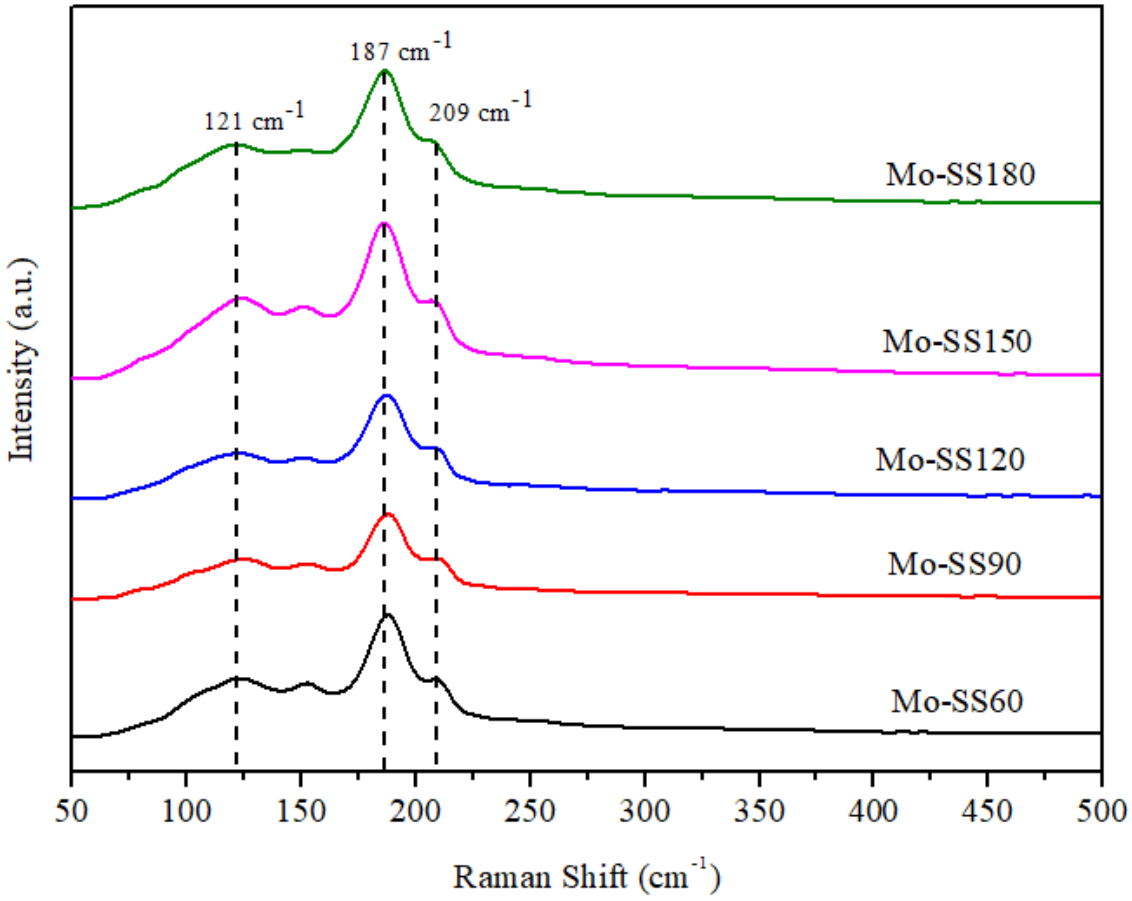

Figure 4.5. Raman shifts of the Mo-SS60, Mo-SS90, Mo-SS120, Mo-SS150, and Mo-SS180

Fig. 4.6 presents the surface morphologies of the TK-Sb_2Se_3 on SLG that are named SS60, SS90, SS120, and SS150 at different t_{Se}. The effect of the t_{Se} on grain shapes and size is understood clearly by the investigation of SEM images at 2 μm scale. Grains of the sample which are selenized at t_{Se} equal to 60 min are stacked horizontally on the substrate surface. When the t_{Se} has increased, grains start to grow vertically on the substrate surface. Grains get nano rod-like shapes that are distributed more uniformly when t_{Se} is equal to 150 min. However, due to the SEM images of the SS150, grains that have rod-like shapes start to get horizontally form.

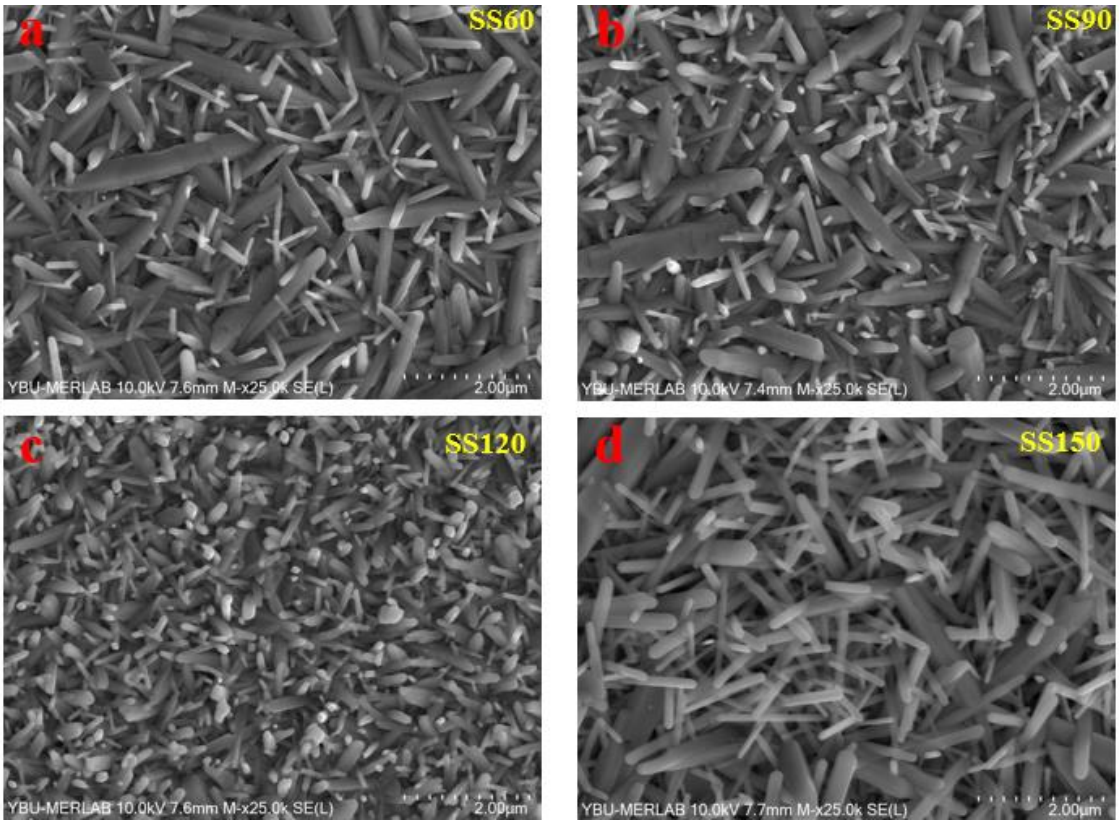

Figure 4.6. SEM images of the a) SS60, b) SS90, c) SS120, and d) SS150

Fig. 4.7 represents SEM images of the TK-Sb_2Se_3 on SLG/Mo in 4 μm scale. When SEM images of the samples are examined, small grains have been observed at Mo-SS60. By the increasing of t_{Se}, grains have been getting bigger and rod-like shapes. Grains of Mo-SS90, Mo-SS120, and Mo-SS150 have been stacked on SLG/Mo substrate horizontally. When t_{Se} is increased to 180 min at Mo-SS180, grains have been getting more vertical form. The grain size distribution of Mo-SS180 is more uniform from the other samples.

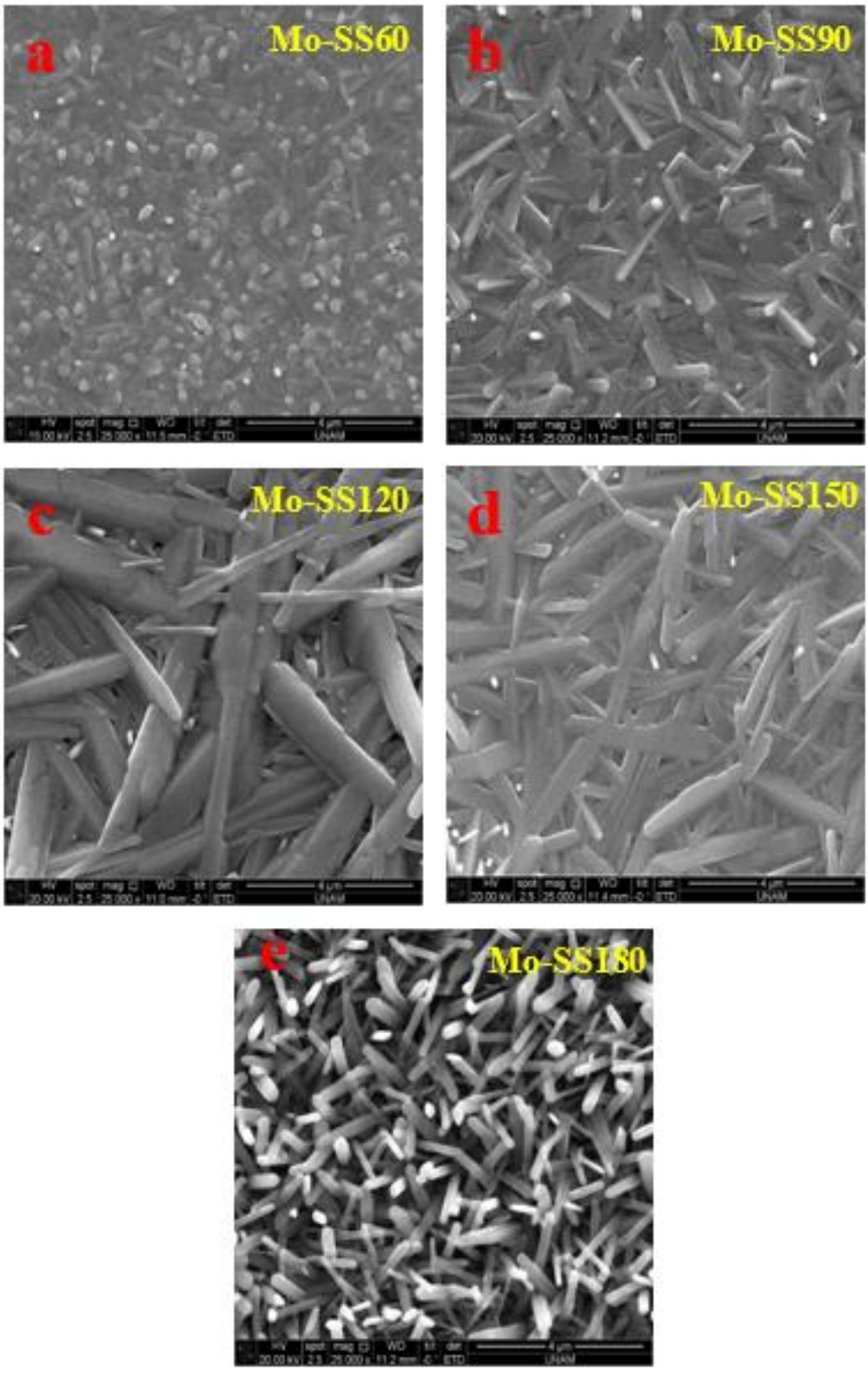

Figure 4.7. SEM images of the a) Mo-SS60, b) Mo-SS90, c) Mo-SS120, d) Mo-SS150, and e) Mo-SS180

According to the SEM images and XRD results of the selenized samples that are TK-Sb_2Se_3 on SLG, aim of the understanding morphology growth of the Sb_2Se thin films with two-step method that is used in this study, FIB-SEM method has been used to examine the cross-section of the sample SS150 which has been achieved complete selenization. According to Fig. 4.8, increasing thickness of the sample SS150 is observed after the selenization in reference to the thickness of the Sb precursor thin film. Due to SEM and FIB-SEM images, rod-shaped grains are not stacked on the substrate surface exact vertically. Those grains are grown on the substrate surface compactly for a while time but by increasing t_{Se}, the growth direction of rod-shaped grains is getting horizontally. FIB-SEM cross-section image of SS150, the thickness of the structure has reached above ~800 nm with rod-shaped structure. ~790 nm part of the structure that is in contact with substrate surface has grown compactly.

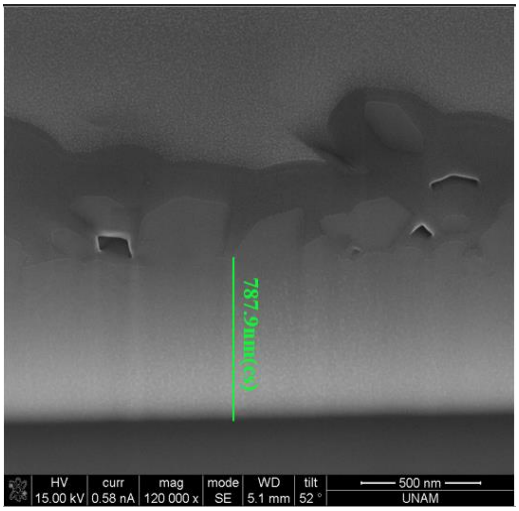

Figure 4.8. FIB-SEM cross-section image of SS150

In Fig. 4.9, XPS spectra of SS150 and atomic concentration vs. etching time graph of Mo-SS180 is given. When XPS spectra of the SS150 is examined, it includes peaks that are substantially matched with binding energies of Sb and Se. Binding energy of Sb $3d_{3/2}$ and Sb $3d_{5/2}$ are 538.40 eV and 529.06 eV and binding energy of Se $3d_{3/2}$ and Se $3d_{5/2}$ are 54.84 eV and 53.86 eV respectively. Due to the peak positions, it is clear that there are no impurity states in SS150. The survey spectrum of SS150 is very similar to the previous study which is published by Shen et al [51]. When the graph is examined which is belong to Mo-SS180, depending on the etching time, the depletion of Sb and Se elements is

simultaneous in the structure. The increasing atomic concentration of Mo also match with the decreasing atomic concentration of the other elements.

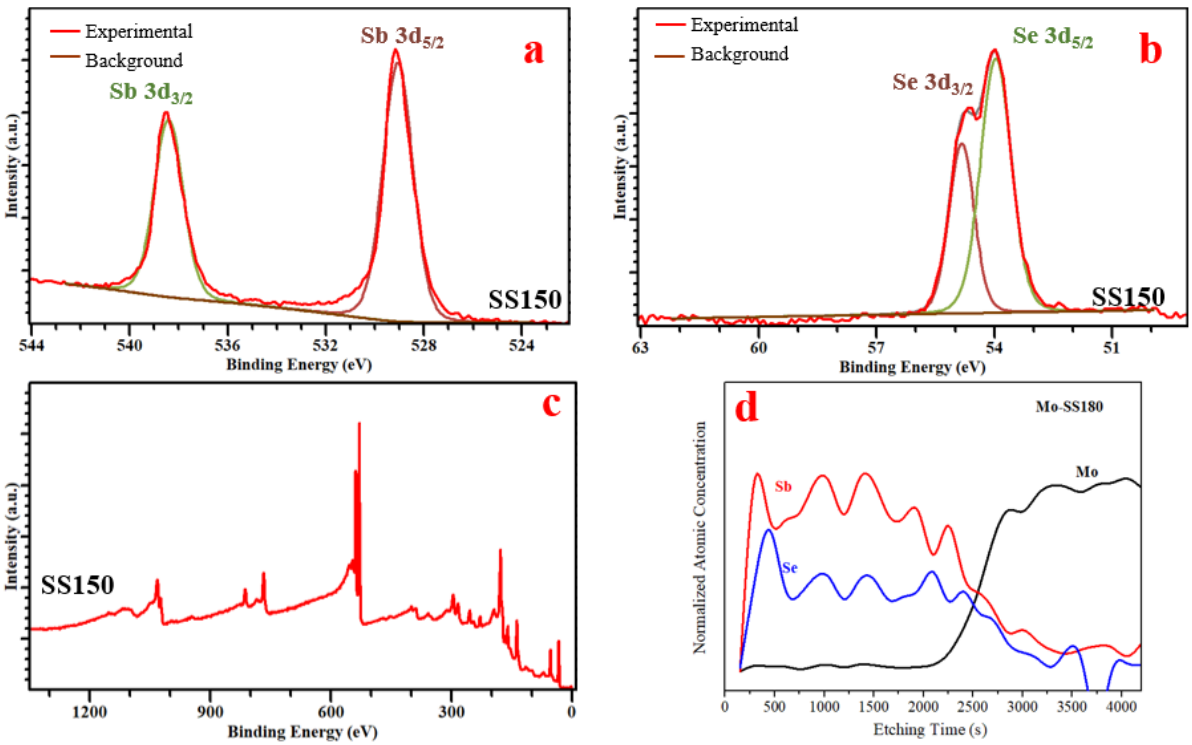

Figure 4.9. XPS spectra of SS150 a) Sb 3d, b) Se 3d peaks, c) survey spectra of SS150 and d) normalized atomic concentration graph of Mo-SS180 versus etching time

EDS results of the samples which are complete selenized samples on SLG and SLG/Mo substrate have been given in Table 4.1. Neither SS150 nor Mo-SS180 is close to the stoichiometric percentage of the Sb_2Se_3 structure that is composed of 60% Se-40% Sb atoms.

Table 4.1. EDS results of the SS150 and Mo-SS180

	Atomic %		Atomic Sb/Se
	Sb	Se	
SS150	43.29	56.71	0.76
Mo-SS180	43.94	56.06	0.78

Fig. 4.10 represents the PL spectroscopy of the SS150 and Mo-SS180. The single and sharp lines have been obtained by PL spectra. The center of the peaks is positioned at around 1.53 eV. PL is a defect sensitive technique and the large FWHM value of the PL peak attributes to the surface defects. FWHM values of the PL spectra of both SS150 and Mo-SS180 are 2.8 nm.

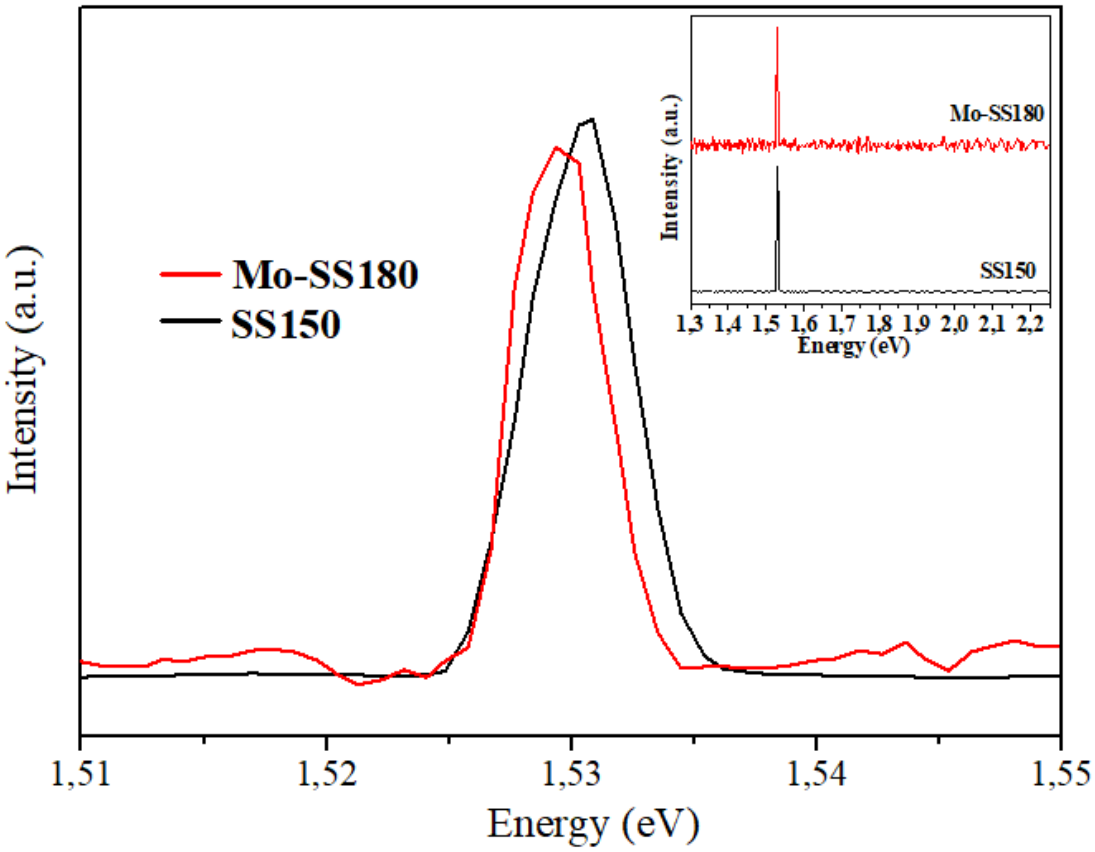

Figure 4.10. PL spectra of the SS150 and Mo-SS180, inset: Full PL spectra of the SS150 and Mo-SS180

4.2.2. TN-Sb_2Se_3 on SLG and SLG/Mo

XRD patterns of the TN-Sb_2Se_3 on SLG samples are indicated in Fig. 4.11. All diffraction peaks of the samples have been matched with orthorhombic Sb_2Se_3 structure completely. Any secondary phase has not been detected from the XRD patterns of the samples. When

the XRD pattern of S60 is examined, dominant peak orientations of S60 are (130), (230), (240), and (002). When t_{Se} is increased respectively to 90, 120 and 150 min, the orientation of dominant peaks has been changed. S120 have (211), (221), and (002) oriented diffraction peaks. The intensity of these peaks is higher at S150 when t_{Se} has reached 150 min.

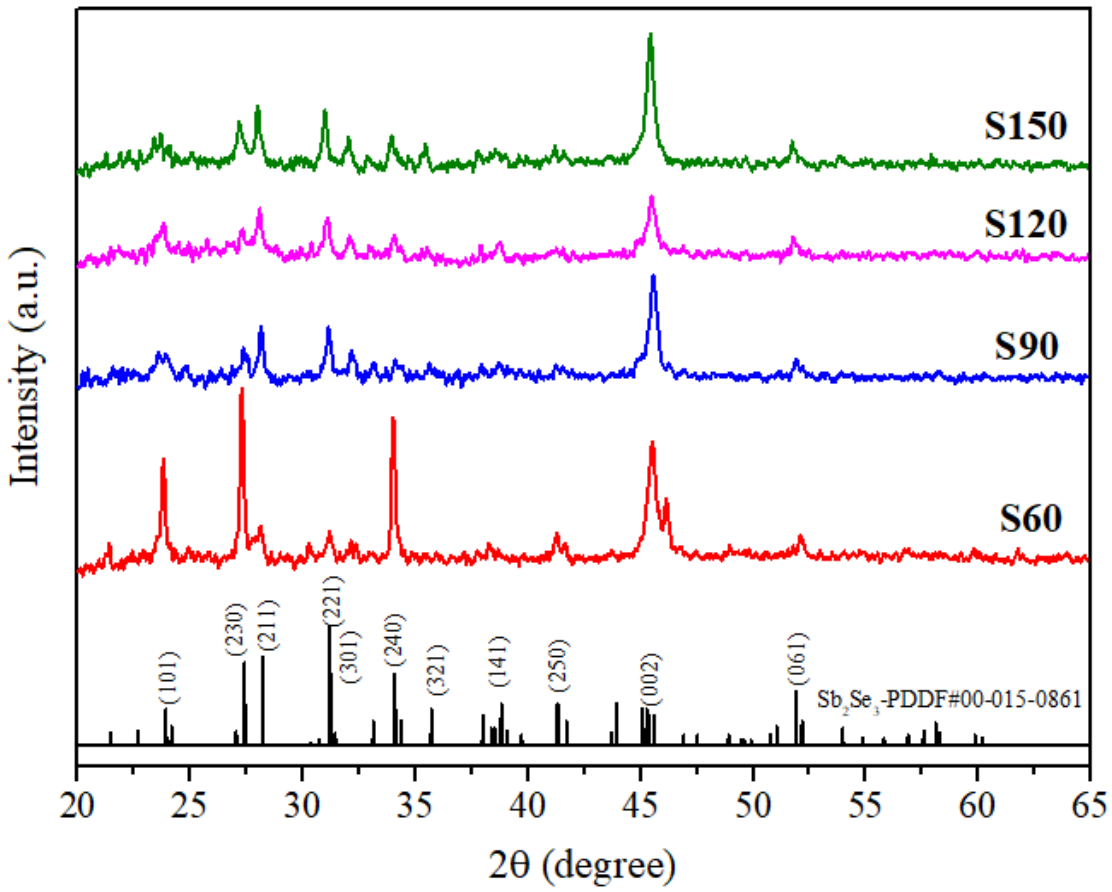

Figure 4.11. XRD patterns of the S60, S90, S120, and S150

Fig. 4.12 represents the XRD patterns of the TN-Sb_2Se_3 on SLG/Mo at different t_{Se}. Diffraction peaks of the TN-Sb_2Se_3 on SLG/Mo are completely matched with orthorhombic Sb_2Se_3 structure and include Mo (110). When the XRD pattern of Mo-S60 is examined, (002) oriented peak is dominant. By the increasing of t_{Se}, the orientation of the dominant peak has been changed. The most dominant peaks of Mo-S90 and Mo-S120 are (230), (240), and (002) oriented. When t_{Se} is reached 150 min, (211), (221), and (002) oriented peaks have gotten dominantly.

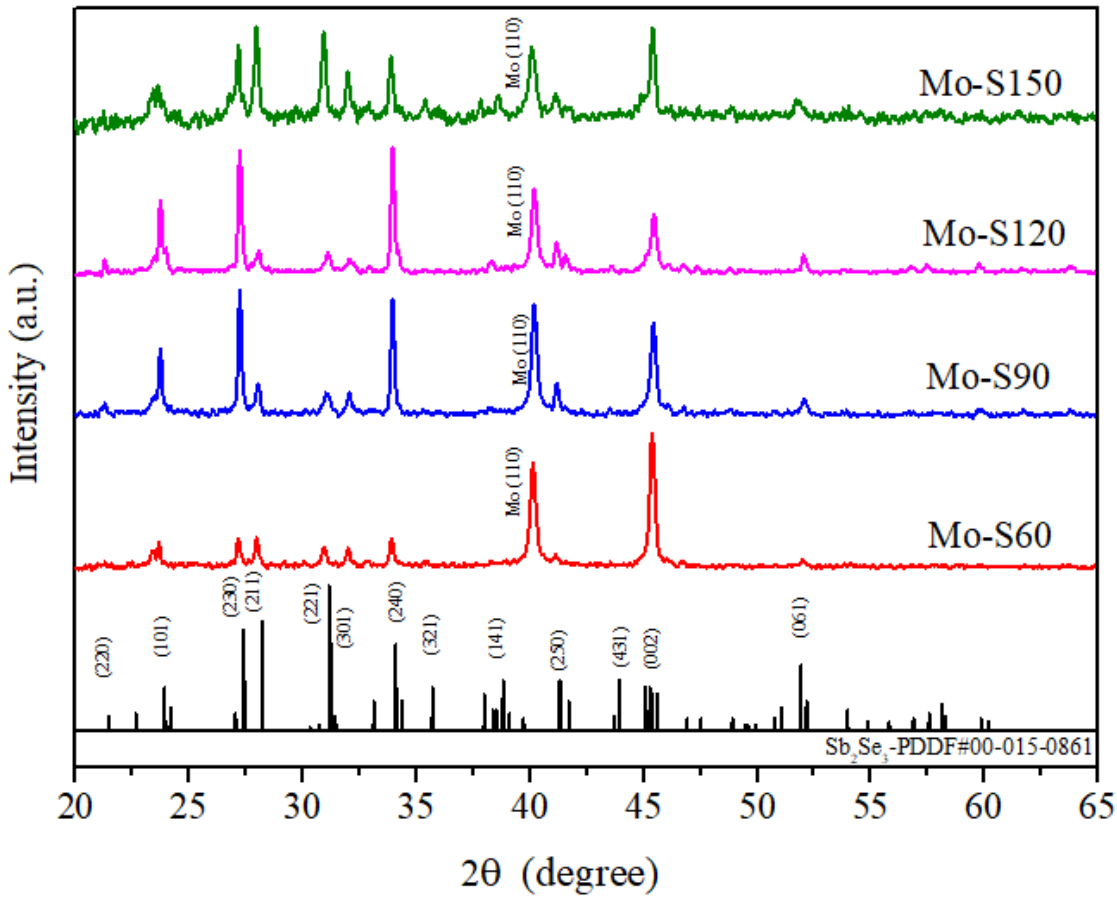

Figure 4.12. XRD patterns of the Mo-S60, Mo-S90, Mo-S120, and Mo-S150

In Figure 4.13 Raman spectra of TN-Sb_2Se_3 on SLG are represented. As in the samples whose Raman data have been given previously, all samples have a significant peak of around 187 cm^{-1} and two weak peaks around 121 cm^{-1} and 207 cm^{-1}. Any peak which belongs to the undesired secondary phase has not been detected.

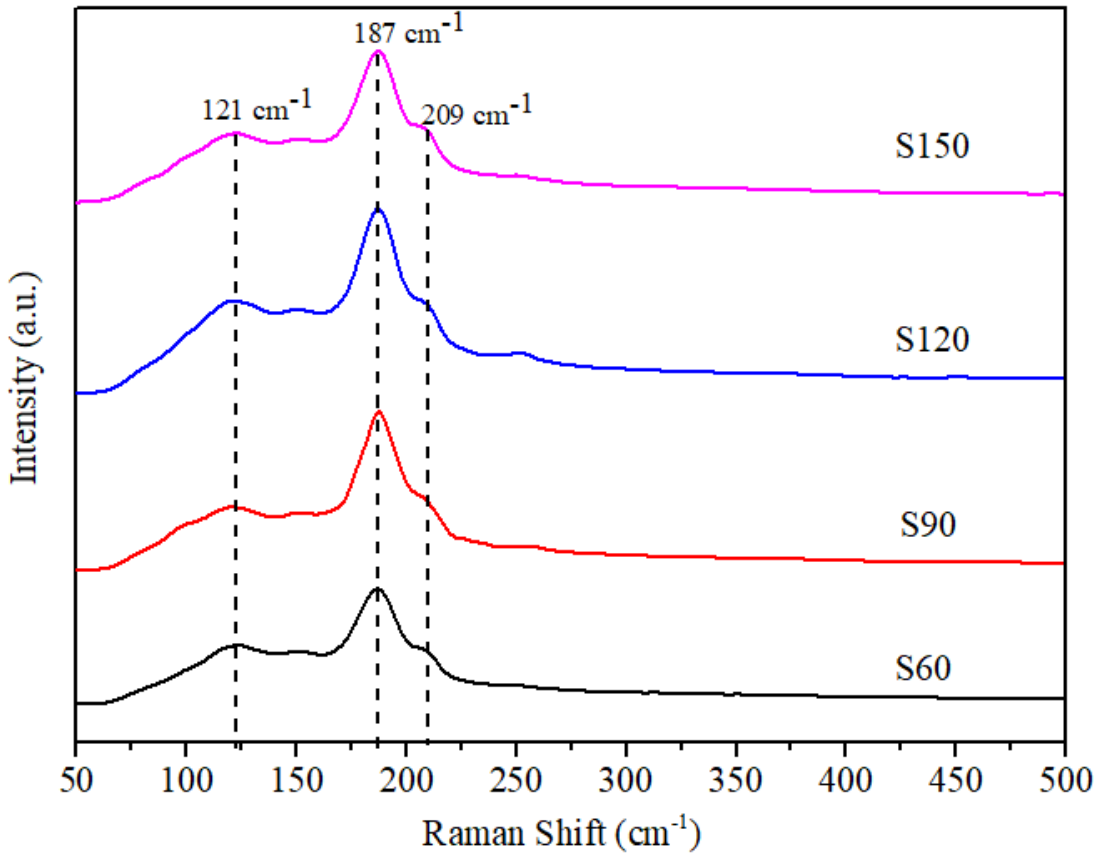

Figure 4.13. Raman shifts of the S60, S90, S120, and S150

Raman shifts of TN-Sb_2Se_3 on SLG/Mo have been shown in Fig. 4.14. Raman shifts that belong to the orthorhombic Sb_2Se_3 structure have been clearly observed. All samples have peaks of around 187 cm^{-1}, 121 $cm^{-1,}$ and 207 cm^{-1} that have been assigned orthorhombic Sb_2Se_3. Depending on the absence of the Mo layer, this type of structure can include some secondary phases. Fortunately, there are no unwanted secondary phases in all TN-Sb_2Se_3 on SLG/Mo.

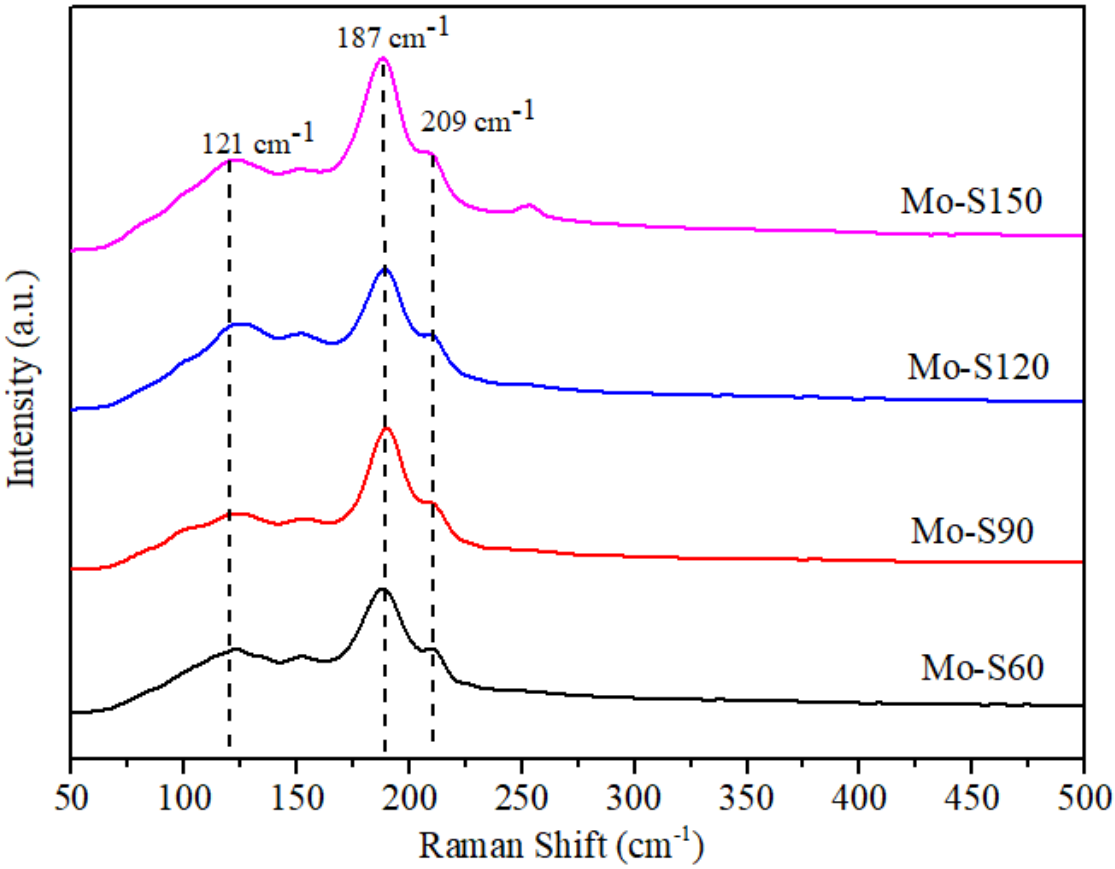

Figure 4.14. Raman shifts of the Mo-S60, Mo-S90, Mo-S120, and Mo-S150

SEM images of the TN-Sb_2Se_3 on SLG samples are presented in Fig. 4.15 at 2 μm scale. Surface morphologies of the samples have changed at different t_{Se}. All samples have rod-like grain shapes, but the grain size distribution and growth direction of the samples have not similar to each other. When surface morphology of TN-Sb_2Se_3 on SLG has been compared with TK- Sb_2Se_3 on SLG and SLG/Mo, this group has more vertical rod-like grains. It has been observed that S60 has the smallest grains. When the surface morphology of S120 has been compared to the other samples, S120 has the biggest grain size in this sample group. The grain size of the S150 sample has started to get smaller when t_{Se} has been increased to 150 min.

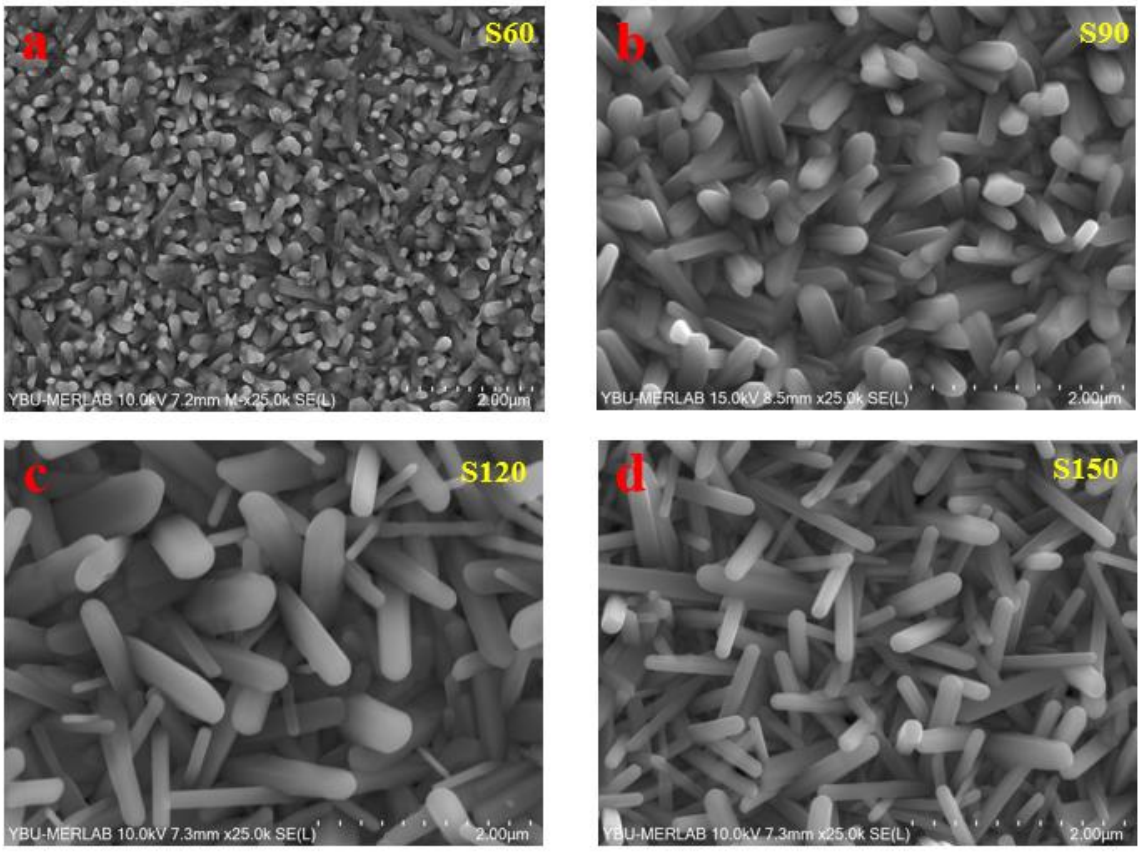

Figure 4.15. SEM images of the a) S60, b) S90, c) S120, and d) S150

SEM images of TN-Sb_2Se_3 on SLG/Mo in 2 µm scale are shown in Figure 4.16 . When SEM images of Mo-S60, Mo-S90, and Mo-S120 have been examined, these samples have nonuniform grain size distribution and horizontal grains to substrate surface. On the contrary of this situation, when t_{Se} has reached 150 min, the surface morphology of Mo-S150 has turned uniformly distributed rod-like grains which are similar to S150.

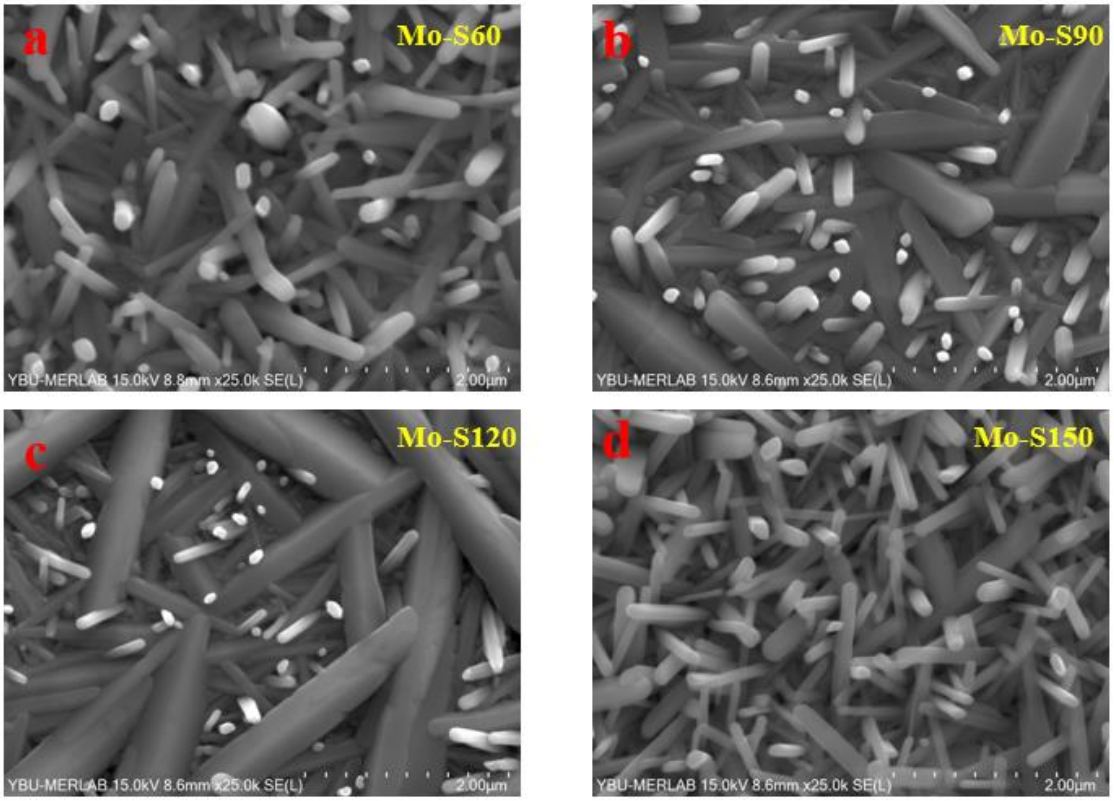

Figure 4.16. SEM images of the a) Mo-S60, b)Mo- S90, c) Mo-S120, and d)Mo- S150

In Fig. 4.9, XPS spectra of S150 and atomic concentration vs. etching time graph of Mo-S150 is given. When XPS spectra of the S150 is examined, it has determined that the binding energy of Sb $3d_{3/2}$ and Sb $3d_{5/2}$ are 538.80 eV and 529.47 eV and binding energy of Se $3d_{3/2}$ and Se $3d_{5/2}$ are 55.27 eV and 54.36 eV respectively. These binding energy values have matched with the binding energies of Sb and Se. Peak positions of Sb and Se of S150 have proved that there is no impurity state in this sample. Survey spectra of S150 have matched the literature. When the graph is examined which is belongs to Mo-S150, the increasing atomic concentration of Mo also has matched with the decreasing atomic concentration of the other elements.

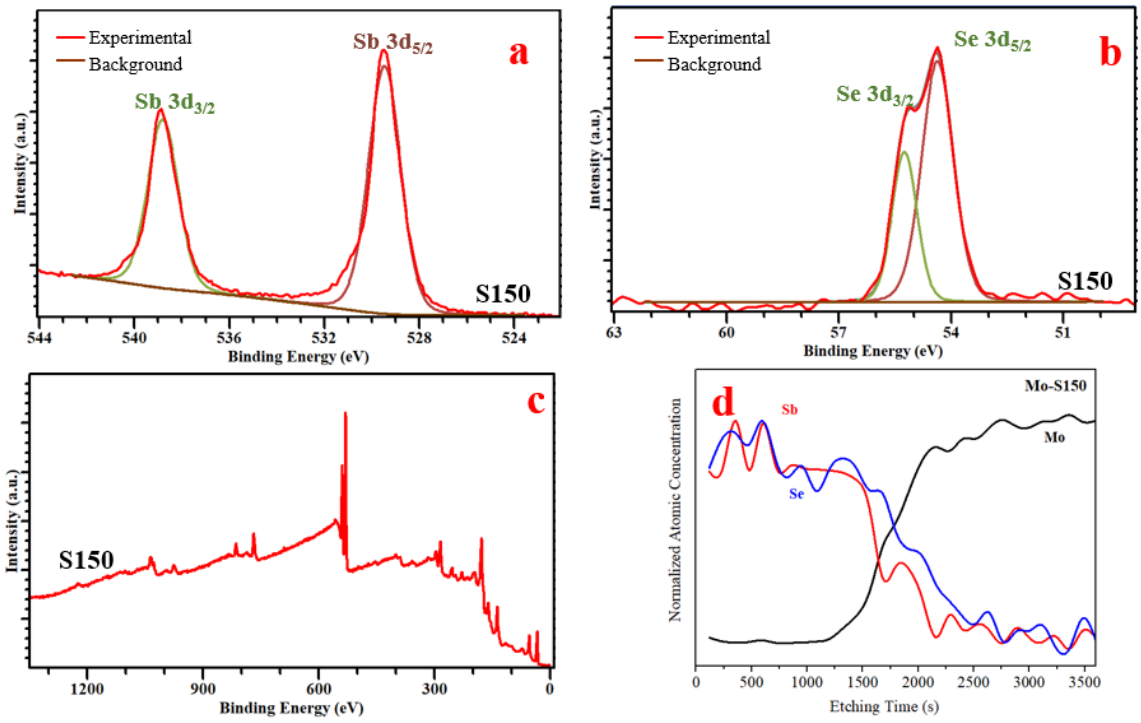

Figure 4.17. XPS spectra of S150 a) Sb 3d, b) Se 3d peaks, c) survey spectra of S150 and d) normalized atomic concentration graph of Mo-S150versus etching

EDS results of the samples which are S150 and Mo-S150 have been given in Table 4.2. When the stoichiometric percentage of the S150 has been examined, this sample is not close to the stoichiometric percentage of the Sb_2Se_3 structure that is composed of 60 % Se-40 % Sb atoms. Therefore, Mo-S150 has reached this stoichiometric percentage value very closely.

Table 4.2. EDS results of the S150 and Mo-S150

	Atomic %		Atomic Sb/Se
	Sb	Se	
S150	44.00	56.00	0.78
Mo-S150	40.60	59.40	0.68

Fig. 4.18 represents the PL of the S150 and Mo-S150. The single and sharp lines have been obtained by PL spectra. The center of the peaks is positioned at around 1.53 eV which is the same as SS150 and Mo-SS180. FWHM values of the PL spectra of S150 and Mo-S150 are respectively 2.9 nm and 3.0 nm.

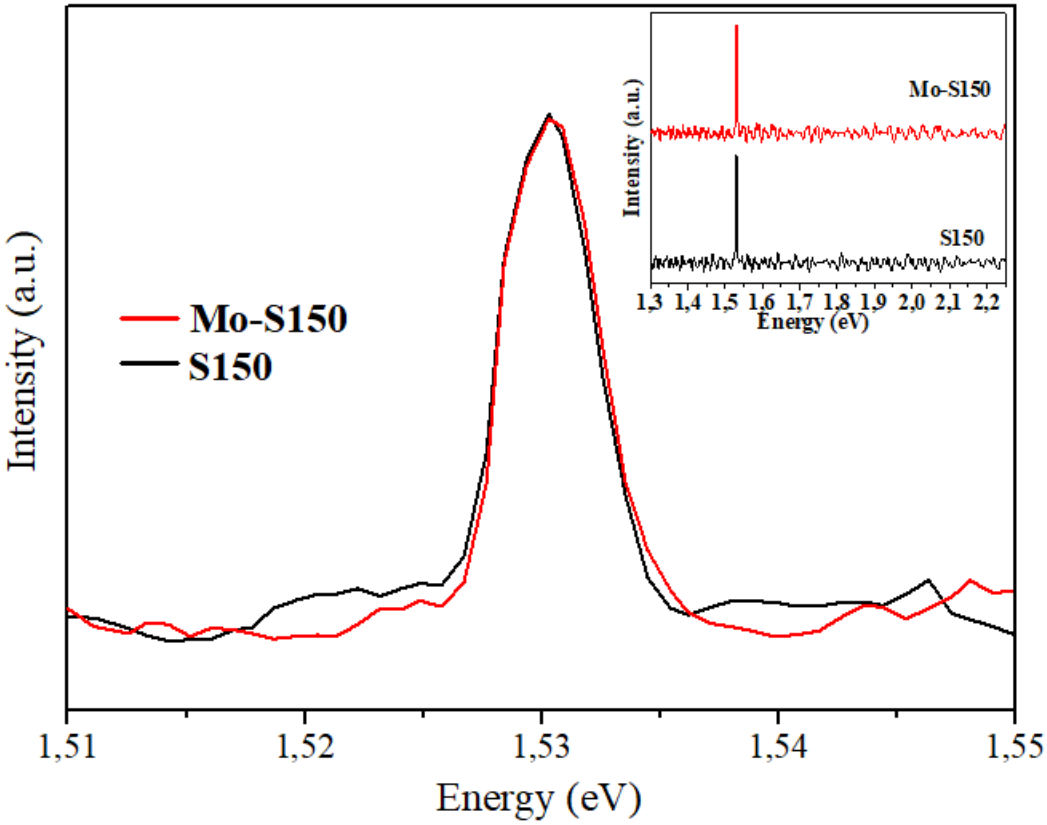

Figure 4.18. PL spectra of the S150 and Mo-S150, inset: Full PL spectra of the S150 and Mo-S150

5. DISCUSSION

In this thesis, synthesis of Sb_2Se_3 thin film structure by two-step production, characterization of produced thin film, and determining the advantages and disadvantages of the method in terms of photovoltaic properties according to the characterization results have been aimed. Due to these purposes, Sb_2Se_3 thin films have been synthesized by two-step production which includes sputtering metallic precursor and selenization step.

RF magnetron sputtering method has been used for deposition of Sb precursors and deposition parameters have been optimized. Sb precursors have been deposited on SLG and SLG/Mo substrates as ~250 and ~500 nm thickness Depending on these, after the selenization step, effects of deposition on different structures and effects of precursor thickness on structural and morphological growth of thin film can be examined. For the selenization step, one zone tubular furnace has been used and selenization parameters have been optimized. Selenization of deposited Sb precursor has been performed at different $t_{Se.}$ Due to different t_{Se}, the effect of different t_{Se} structural growth of thin film can be examined.

Experimental studies of this thesis have been started with selenization of thick Sb metallic thin film precursors which have ~500 nm thickness. When the XRD patterns of selenized thick Sb precursor that are selenized at different t_{Se} are examined, SS60, SS90, and SS120 have different a peak that belongs to Sb (110) from orthorhombic Sb_2Se_3 structure. The uncontrolled existence of the secondary phase in the thin film structure causes decreasing efficiency value of the material. Sb (110) has been eliminated when t_{Se} is increased to 150 min at SS150.

(hk1) and (hk2) oriented Sb_2Se_3 structure that is dominantly (221) and (211) orientations show good carrier transport performance due to strong covalent bonds between Sb-Se atoms. (hk0) oriented grains are stacking on the substrate surface horizontally and bonded with weak Van der Waals bonds, so dangling bonds and grain boundaries cause poor carrier transport performance due to the recombination [40]. When the XRD patterns of selenized thick Sb thin films that are selenized at different t_{Se} are examined, the most dominant peak is (002) in the structure of the SS150 that is selenized completely. However, results of the SEM and FIB-SEM

have shown that the sample consisted of rod-like shaped grains with horizontal orientations that can negatively affect the carrier transport performance [50] and that the sample thickness increased after selenization depending on the diffusion of Se atoms. Considering the carrier transportation mechanism of thin film solar cells, the horizontally growing of the grains reduces the carrier transportation performance due to the high serial resistivity. Due to the FIB-SEM data, rod-shaped grains are not stacked on the substrate surface exactly vertically depending on the long $t_{Se,}$ and those grains which are ~790 nm thick part of the structure that is in contact with substrate surface have grown on the substrate surface compactly for a while time but by increasing t_{Se}, the growth direction of rod-shaped grains have gotten horizontally. The thickness of the structure has reached above ~800 nm with a rod-shaped structure. It is known that an excess increment of the thickness of the absorber layer could cause the go-up recombination

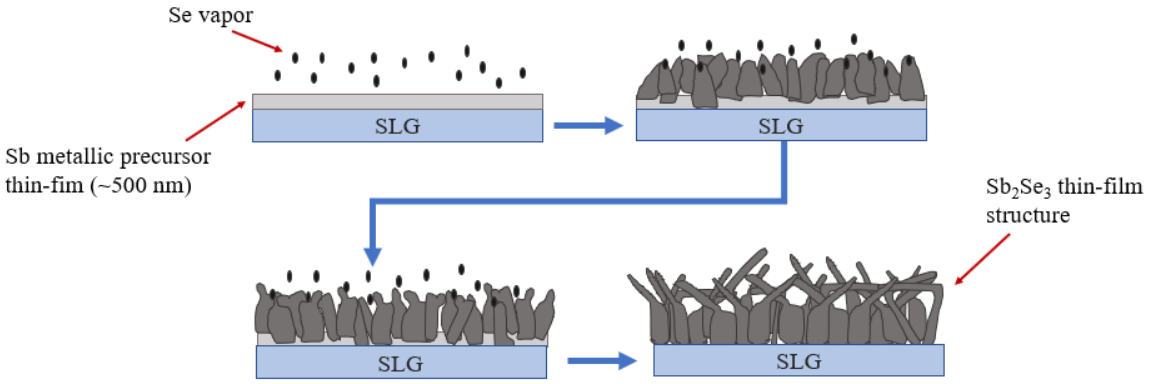

Figure 5.1. Schematic illustration of growth model of Sb_2Se_3 thin film that is obtained from selenization of ~500 nm thick Sb metallic precursor thin films

probability of charge carriers. In Figure 5.1. grain growth of the structure is schematized.

Mo thin films are widely used as a back contact material for PV applications, so morphological and structural growth of SbSe thin films on Mo thin films has to be suitable for solar cells. Because of this situation, Sb metallic precursors have been deposited on Mo thin films and selenized. When surface morphology of TK-Sb on SLG/Mo, it has been determined that the average grain size of thick metallic Sb precursor deposited on SLG/Mo substrate is larger than the average grain size of the thick metallic Sb precursor deposited on SLG substrate. Therefore, t_{Se} has reached 180 min in TK-Sb on SLG/Mo as opposed to TK-Sb on SLG. When examination

of characterization results of the TK-Sb_2Se_3 on SLG/Mo, all data that are obtained from XRD, SEM is almost similar to TK-Sb_2Se_3 on SLG. Mo-SS60, Mo-SS90, Mo-SS120, and Mo-SS150 have metallic Sb in their structure which is determined by XRD. Sb (110) has been eliminated when t_{Se} reaches to 180 min at Mo-SS180. Due to the XRD pattern of the Mo-SS180, the intensity of the (hk0) oriented peaks has decreased. When SEM images of the samples are compared to each other, Mo-SS180 grains have been getting more vertical form. However, deposition of Sb precursors on different structures as SLG and SLG/Mo has not caused significant structural changes at grain growth. At this stage, for preventing excess thickness increment of Sb_2Se_3 thin film structure and limiting the growth after compact layer, the thickness of Sb precursor metallic thin film has been decreased ~500 nm to ~250 nm.

When XRD patterns of the TN-Sb_2Se_3 on SLG have been examined, unlike the other selenized group samples, any diffraction peak except Sb_2Se_3 has not been observed. S60 has (hk0) oriented dominant peaks. By the increasing of the t_{Se}, the intensity of the (hk1) and (hk2) oriented peaks which are benign for carrier transport have increased. SEM images of TN-Sb_2Se_3 on SLG have been indicated different grain characteristics. S60 has significantly more vertically oriented and homogenously distributed grains than the other samples that can be benign for carrier transport performance. But XRD pattern of S60 has dominantly (hk0) oriented peaks which decreases carrier transport performance. By the increasing of the $t_{Se,}$ grain sizes of the TN-Sb_2Se_3 on SLG have increased.

When the XRD pattern of the TN-Sb_2Se_3 on SLG/Mo has been examined, the peaks of the Sb_2Se_3 structure enhanced compared to the other samples and the most dominant peaks are (211), (221), and (002) oriented in this structure. SEM image Mo-S150 has been examined and there is no obvious change in the surface morphology of this sample due to Mo back contact material.

When comparing XRD patterns of four selenized films which are SS150, Mo-SS180, S150, and Mo-S150, S150 and Mo-S150 have more significant (211) and (221) oriented peaks than SS150 and Mo-SS180. According to the $I_{(211)}/I_{(002)}$ and $I_{(221)}/I_{(002)}$ ratios that have been given in Table 5.1, it has proven that the (hk1) oriented peaks in S150 and Mo-S150 are more distinct than in SS150 and Mo-SS180. Crystallite sizes have been determined from the XRD patterns of SS150, Mo-SS180, S150, and Mo-S150. The Scherrer method has been used for calculating the average crystallite size of SS150, Mo-S180, S150, and Mo-S150 that are given in Table 5.1. When the XRD pattern of the Mo-S150 has been examined, the peaks of the Sb_2Se_3 structure enhanced compared to the other samples and the most dominant peaks are (211), (221), and (002) oriented in this structure. According to Table 5.1, the ratio $I_{(211)}/I_{(002)}$ and $I_{(221)}/I_{(002)}$ have reached the maximum in Mo-S150.

Table 5.1. $I_{(211)}/I_{(002)}$ and $I_{(221)}/I_{(002)}$ ratios and crystallite sizes of SS150, Mo-SS180, S150, and Mo-S150

	$I_{(211)}/I_{(002)}$	$I_{(221)}/I_{(002)}$	Crystallite Size (nm)
SS150	0.19	0.12	31.00
Mo-SS180	0.35	0.25	32.30
S150	0.56	0.55	30.80
Mo-S150	0.99	0.95	70.63

Raman spectra of all samples have been performed for the further investigation of crystalline phases. Both three samples that are SS150, Mo-SS180, S150, and Mo-S150 have a significant peak of around 187 cm^{-1} and two weak peaks around 121 cm^{-1} and 207 cm^{-1}. All peaks directly match with orthorhombic Sb_2Se_3 and the peaks at 187 cm^{-1} and 207 cm^{-1} are assigned to the heteropolar Sb-Se bond vibrations. In addition to these, according to the Raman spectra of Mo-SS180 and Mo-S150, there is no uncontrolled secondary phase formation such as $MoSe_2$. $MoSe_2$ is formed at a high temperature of about 550℃ in the Se vapor atmosphere, but it was also observed that occurs under 550℃ [72]. $MoSe_2$ forms a good ohmic contact between Mo back contact material and the Sb_2Se_3 thin film by the virtue of its formation at a certain thickness [45, 53]. However, uncontrolled secondary phase formation can limit the solar cell device performance [73, 74]. Since the complete selenization of the Sb thin films that have been

deposited on SLG/Mo have been carried out at a relatively low temperature of 250℃, uncontrolled formation of secondary phases such as $MoSe_2$ has been prevented.

In this thesis, XPS has been performed for investigating the purity of chemical states of SS150 and S150 and also examination of elemental atomic concentration changes of Mo-SS180 and Mo-S150 versus etching time. When XPS spectra of the SS150 and S150 have been examined, impurity states such as oxygen which causes chemical state changes and affects the binding energies of Sb and Se have not been detected. When atomic concentration changes of elements that belong to Mo-SS180 and Mo-S150 due to the etching time have been examined, the increasing atomic concentration of Mo has also matched with the decreasing atomic concentration of the other elements. It is clear that Sb and Se have not been found separately in the depth profile of Mo-SS180 and Mo-S150. This situation has eliminated the possibility of unwanted secondary phase formation in the structure.

It has been understood that Mo-S150 has a similar stoichiometric percentage to the Sb_2Se_3 structure by EDS. The atomic Sb/Se ratio of the Sb_2Se_3 structure is 0.66 and Mo-S150 which has a 0.68 atomic Sb/Se ratio is very close to this value. Depending on the long $t_{Se,}$ Se atoms can be back-evaporated from the thin film surface locally so, the atomic ratio of Sb atoms can be high at the other samples which are SS150, Mo-SS180, and S150.

The optical properties of SS150, Mo-SS180, S150, and Mo-S150 have been determined by PL that is defect sensitive technique. The large full width half maximum (FWHM) value which is obtained from PL spectra is attributed to surface defects. The center of the peaks is positioned at 1.53 eV which value belongs to the synthesized Sb_2Se_3 thin films. The single and sharp lines have been obtained by PL spectra. When FWHM values of these samples have been compared, it has been determined that there are no significant differences between them. Due to these FWHM values, defect density analysis of samples is meaningless. For the first time, the PL spectroscopy of the samples whose surface morphology has included rod-shaped grains has been investigated in this thesis.

As a summary of this thesis, for synthesizing of Sb_2Se_3 thin films, Sb metallic precursor thin films have been deposited on SLG and SLG/Mo substrate successfully by RF magnetron

sputtering technique with two different thicknesses and selenized in single zone tubular furnace with different selenization time. For achieving complete selenization of Sb metallic precursor at low T_{Se} with suitable crystal structure and morphology for PV applications, the effect of t_{Se} and thickness of precursor thin film have been studied. By increasing the t_{Se}, the precursor films have been completely selenized. In addition, by reducing the thickness of the precursor film, a structurally and morphologically more suitable SbSe thin film for PV applications has been obtained. Thanks to the lowest selenization temperature in literature, uncontrolled secondary phase formation has not been observed between Mo back contact material. In the light of these results, it is hoped that the study will contribute to future studies of SbSe thin film absorber layer.

6. REFERENCES

[1] V.V. Quaschning, Renewable energy and climate change, John Wiley & Sons2019.

[2] B. Looney, BP statistical review of world energy, BP Statistical Review: London, UK, 2020.

[3] Enerji Piyasası Düzenleme Kurumu, Doğal Gaz Piyasası 2019 Yılı Sektör Raporu Listesi

[4] P.A. Owusu, S. Asumadu-Sarkodie, A review of renewable energy sources, sustainability issues and climate change mitigation, Cogent Engineering, 3 (2016) 1167990.

[5] Enerji ve Tabii Kaynaklar Bakanlığı, Tabii Kaynaklar, Kömür

[6] J.P. Dorian, H.T. Franssen, D.R. Simbeck, Global challenges in energy, Energy policy, 34 (2006) 1984-1991.

[7] NASA Global Climate Change, Carbon Dioxide, 2021.

[8] J. Goldemberg, World energy assessment. Energy and the challenge of sustainability, (2001).

[9] E.E.S. Michaelides, Alternative energy sources, Springer Science & Business Media2012.

[10] F.A. Farret, M.G. Simoes, Integration of alternative sources of energy, John Wiley & Sons2006.

[11] Electromagnetic Spectrum

[12] P. Hersch, K. Zweibel, Basic photovoltaic principles and methods, Solar Energy Research Inst., Golden, CO (USA), 1982.

[13] Z. Sen, Solar energy fundamentals and modeling techniques: atmosphere, environment, climate change and renewable energy, Springer Science & Business Media2008.

[14] California’s new solar power plant is actually a death ray that’s incinerating birds mid-flight.

[15] S. Albrecht, B. Rech, Perovskite solar cells: On top of commercial photovoltaics, Nature Energy, 2 (2017) 1-2.

[16] K.-D. Jäger, O. Isabella, A.H. Smets, R.A. van Swaaij, M. Zeman, Solar energy: fundamentals, technology and systems, UIT Cambridge2016.

[17] C.M. Hussain, Handbook of nanomaterials for industrial applications, Elsevier2018.

[18] K. Ranabhat, L. Patrikeev, A. Antal'evna-Revina, K. Andrianov, V. Lapshinsky, E. Sofronova, An introduction to solar cell technology, Journal of Applied Engineering Science, 14 (2016) 481-491.

[19] M. Imamzai, M. Aghaei, Y.H.M. Thayoob, M. Forouzanfar, A review on comparison between traditional silicon solar cells and thin-film CdTe solar cells, Proceedings of National Graduate Conference (Nat-Grad, 2012, pp. 1-5.
[20] K. Chopra, P. Paulson, V. Dutta, Thin-film solar cells: an overview, Progress in Photovoltaics: Research and applications, 12 (2004) 69-92.
[21] D. Abou-Ras, T. Kirchartz, U. Rau, Advanced characterization techniques for thin film solar cells, Wiley Online Library2011.
[22] A. Romeo, E. Artegiani, CdTe-Based Thin Film Solar Cells: Past, Present and Future, Energies, 14 (2021) 1684.
[23] A.M. Ali, K. Rahman, L.M. Ali, M. Akhtaruzzaman, K. Sopian, S. Radiman, N. Amin, A computational study on the energy bandgap engineering in performance enhancement of CdTe thin film solar cells, Results in physics, 7 (2017) 1066-1072.
[24] K. Mitchell, A.L. Fahrenbruch, R.H. Bube, Photovoltaic determination of optical-absorption coefficient in CdTe, Journal of Applied Physics, 48 (1977) 829-830.
[25] C.S. Tao, J. Jiang, M. Tao, Natural resource limitations to terawatt-scale solar cells, Solar Energy Materials and Solar Cells, 95 (2011) 3176-3180.
[26] S.-W. Cho, A.-H. Kim, G.-A. Lee, C.-W. Jeon, Quantification of the Contact Resistance of ZnO/MoSe 2/Mo Contact Formed in a Monolithic CIGS Photovoltaic Module, Electronic Materials Letters, (2021) 1-6.
[27] S. Jung, S. Ahn, J.H. Yun, J. Gwak, D. Kim, K. Yoon, Effects of Ga contents on properties of CIGS thin films and solar cells fabricated by co-evaporation technique, Current Applied Physics, 10 (2010) 990-996.
[28] H. Li, F. Qu, H. Luo, X. Niu, J. Chen, Y. Zhang, H. Yao, X. Jia, H. Gu, W. Wang, Engineering CIGS grains qualities to achieve high efficiency in ultrathin Cu (InxGa1− x) Se2 solar cells with a single-gradient band gap profile, Results in Physics, 12 (2019) 704-711.
[29] M. Nakamura, K. Yamaguchi, Y. Kimoto, Y. Yasaki, T. Kato, H. Sugimoto, Cd-free Cu (In, Ga)(Se, S) 2 thin-film solar cell with record efficiency of 23.35%, IEEE Journal of Photovoltaics, 9 (2019) 1863-1867.
[30] H. Xie, M. Dimitrievska, X. Fontané, Y. Sánchez, S. López-Marino, V. Izquierdo-Roca, V. Bermúdez, A. Pérez-Rodríguez, E. Saucedo, Formation and impact of secondary phases in Cu-poor Zn-rich Cu2ZnSn (S1− ySey) 4 (0≤ y≤ 1) based solar cells, Solar Energy Materials and Solar Cells, 140 (2015) 289-298.

[31] W. Wang, M.T. Winkler, O. Gunawan, T. Gokmen, T.K. Todorov, Y. Zhu, D.B. Mitzi, Device characteristics of CZTSSe thin-film solar cells with 12.6% efficiency, Advanced Energy Materials, 4 (2014) 1301465.
[32] J. Kim, H. Hiroi, T.K. Todorov, O. Gunawan, M. Kuwahara, T. Gokmen, D. Nair, M. Hopstaken, B. Shin, Y.S. Lee, High efficiency Cu2ZnSn (S, Se) 4 solar cells by applying a double In2S3/CdS emitter, Advanced Materials, 26 (2014) 7427-7431.
[33] M. He, C. Yan, J. Li, M.P. Suryawanshi, J. Kim, M.A. Green, X. Hao, Kesterite Solar Cells: Insights into Current Strategies and Challenges, Advanced Science, 8 (2021) 2004313.
[34] H.H. Park, R. Heasley, L. Sun, V. Steinmann, R. Jaramillo, K. Hartman, R. Chakraborty, P. Sinsermsuksakul, D. Chua, T. Buonassisi, Co-optimization of SnS absorber and Zn (O, S) buffer materials for improved solar cells, Progress in Photovoltaics: Research and Applications, 23 (2015) 901-908.
[35] P. Sinsermsuksakul, L. Sun, S.W. Lee, H.H. Park, S.B. Kim, C. Yang, R.G. Gordon, Overcoming efficiency limitations of SnS-based solar cells, Advanced Energy Materials, 4 (2014) 1400496.
[36] S. Di Mare, D. Menossi, A. Salavei, E. Artegiani, F. Piccinelli, A. Kumar, G. Mariotto, A. Romeo, SnS thin film solar cells: perspectives and limitations, Coatings, 7 (2017) 34.
[37] C. Chen, W. Li, Y. Zhou, C. Chen, M. Luo, X. Liu, K. Zeng, B. Yang, C. Zhang, J. Han, Optical properties of amorphous and polycrystalline Sb2Se3 thin films prepared by thermal evaporation, Applied Physics Letters, 107 (2015) 043905.
[38] A. Dutta, R. Singh, S.K. Srivastava, T. Som, Tunable optoelectronic properties of radio frequency sputter-deposited Sb2Se3 thin films: Role of growth angle and thickness, Solar Energy, 194 (2019) 716-723.
[39] M. Huang, P. Xu, D. Han, J. Tang, S. Chen, Complicated and unconventional defect properties of the quasi-one-dimensional photovoltaic semiconductor Sb2Se3, ACS applied materials & interfaces, 11 (2019) 15564-15572.
[40] Y. Zhou, L. Wang, S. Chen, S. Qin, X. Liu, J. Chen, D.-J. Xue, M. Luo, Y. Cao, Y. Cheng, Thin-film Sb 2 Se 3 photovoltaics with oriented one-dimensional ribbons and benign grain boundaries, Nature Photonics, 9 (2015) 409-415.
[41] Z. Li, X. Liang, G. Li, H. Liu, H. Zhang, J. Guo, J. Chen, K. Shen, X. San, W. Yu, 9.2%-efficient core-shell structured antimony selenide nanorod array solar cells, Nature communications, 10 (2019) 1-9.

[42] G.-X. Liang, X.-H. Zhang, H.-L. Ma, J.-G. Hu, B. Fan, Z.-K. Luo, Z.-H. Zheng, J.-T. Luo, P. Fan, Facile preparation and enhanced photoelectrical performance of Sb2Se3 nano-rods by magnetron sputtering deposition, Solar Energy Materials and Solar Cells, 160 (2017) 257-262.
[43] X. Wen, C. Chen, S. Lu, K. Li, R. Kondrotas, Y. Zhao, W. Chen, L. Gao, C. Wang, J. Zhang, Vapor transport deposition of antimony selenide thin film solar cells with 7.6% efficiency, Nature communications, 9 (2018) 1-10.
[44] X. Hu, J. Tao, S. Chen, J. Xue, G. Weng, Z. Hu, J. Jiang, S. Chen, Z. Zhu, J. Chu, Improving the efficiency of Sb2Se3 thin-film solar cells by post annealing treatment in vacuum condition, Solar Energy Materials and Solar Cells, 187 (2018) 170-175.
[45] R. Kondrotas, J. Zhang, C. Wang, J. Tang, Growth mechanism of Sb2Se3 thin films for photovoltaic application by vapor transport deposition, Solar Energy Materials and Solar Cells, 199 (2019) 16-23.
[46] O.S. Hutter, L.J. Phillips, K. Durose, J.D. Major, 6.6% efficient antimony selenide solar cells using grain structure control and an organic contact layer, Solar Energy Materials and Solar Cells, 188 (2018) 177-181.
[47] Y. Lai, Z. Chen, C. Han, L. Jiang, F. Liu, J. Li, Y. Liu, Preparation and characterization of Sb2Se3 thin films by electrodeposition and annealing treatment, Applied surface science, 261 (2012) 510-514.
[48] L. Wang, D.-B. Li, K. Li, C. Chen, H.-X. Deng, L. Gao, Y. Zhao, F. Jiang, L. Li, F. Huang, Stable 6%-efficient Sb 2 Se 3 solar cells with a ZnO buffer layer, Nature Energy, 2 (2017) 1-9.
[49] C. Yuan, X. Jin, G. Jiang, W. Liu, C. Zhu, Sb 2 Se 3 solar cells prepared with selenized dc-sputtered metallic precursors, Journal of Materials Science: Materials in Electronics, 27 (2016) 8906-8910.
[50] C. Yuan, L. Zhang, W. Liu, C. Zhu, Rapid thermal process to fabricate Sb2Se3 thin film for solar cell application, Solar Energy, 137 (2016) 256-260.
[51] S. Li, H. Shen, J. Chen, Y. Jiang, L. Sun, A. Raza, Y. Xu, Effect of selenization temperature on the properties of Sb 2 Se 3 thin films and solar cells by two-step method, Journal of Materials Science: Materials in Electronics, 30 (2019) 19871-19879.
[52] G.-X. Liang, Y.-D. Luo, S. Chen, R. Tang, Z.-H. Zheng, X.-J. Li, X.-S. Liu, Y.-K. Liu, Y.-F. Li, X.-Y. Chen, Sputtered and selenized Sb2Se3 thin-film solar cells with open-circuit voltage exceeding 500 mV, Nano Energy, 73 (2020) 104806.

[53] Y.-D. Luo, R. Tang, S. Chen, J.-G. Hu, Y.-K. Liu, Y.-F. Li, X.-S. Liu, Z.-H. Zheng, Z.-H. Su, X.-F. Ma, An effective combination reaction involved with sputtered and selenized Sb precursors for efficient Sb2Se3 thin film solar cells, Chemical Engineering Journal, (2020) 124599.
[54] K. Seshan, Handbook of thin film deposition processes and techniques, William Andrew2001.
[55] Magnetron Sputtering.
[56] K. Wasa, M. Kitabatake, H. Adachi, Thin film materials technology: sputtering of control compound materials, Springer Science & Business Media2004.
[57] J.E. Mahan, Physical vapor deposition of thin films, 2000.
[58] M. Ohring, Materials science of thin films, Elsevier2001.
[59] S. Hashmi, Comprehensive materials processing, Newnes2014.
[60] Y. Leng, Materials characterization: introduction to microscopic and spectroscopic methods, John Wiley & Sons2009.
[61] M. Sardela, Practical materials characterization, Springer2014.
[62] G.M. Crankovic, ASM Handbook, Volume 10:.: Materials Characterization, ASM International1986.
[63] E.N. Kaufmann, Characterization of Materials, 2 Volume Set, 2003.
[64] C.S. Kumar, Raman spectroscopy for nanomaterials characterization, Springer Science & Business Media2012.
[65] N. Yao, Focused ion beam systems: basics and applications, Cambridge University Press2007.
[66] S. Reyntjens, R. Puers, A review of focused ion beam applications in microsystem technology, Journal of micromechanics and microengineering, 11 (2001) 287.
[67] D.A. Skoog, F.J. Holler, S.R. Crouch, Principles of instrumental analysis, Cengage learning2017.
[68] J.F. Watts, J. Wolstenholme, An introduction to surface analysis by XPS and AES, John Wiley & Sons2019.
[69] D. Brandon, W.D. Kaplan, Microstructural characterization of materials, John Wiley & Sons2013.
[70] C.R. Brundle, C.A. Evans, L. Wilson, S. Wilson, G. Wilson, Encyclopedia of materials characterization: surfaces, interfaces, thin films, Gulf Professional Publishing1992.

[71] T.H. Gfroerer, Photoluminescence in analysis of surfaces and interfaces, Encyclopedia of analytical chemistry: applications, theory and instrumentation, (2006).
[72] Z. Li, X. Chen, H. Zhu, J. Chen, Y. Guo, C. Zhang, W. Zhang, X. Niu, Y. Mai, Sb2Se3 thin film solar cells in substrate configuration and the back contact selenization, Solar Energy Materials and Solar Cells, 161 (2017) 190-196.
[73] Ö. Demircioğlu, M. Mousel, A. Redinger, G. Rey, T. Weiss, S. Siebentritt, I. Riedel, L. Gütay, Detection of a MoSe2 secondary phase layer in CZTSe by spectroscopic ellipsometry, Journal of Applied Physics, 118 (2015) 185302.
[74] D. Abou-Ras, G. Kostorz, D. Bremaud, M. Kälin, F. Kurdesau, A. Tiwari, M. Döbeli, Formation and characterisation of MoSe2 for Cu (In, Ga) Se2 based solar cells, Thin Solid Films, 480 (2005) 433-438.